



LUND UNIVERSITY

Adventures of III-V Semiconductor Surfaces

Benter, Sandra

2023

Document Version:

Publisher's PDF, also known as Version of record

[Link to publication](#)

Citation for published version (APA):

Benter, S. (2023). *Adventures of III-V Semiconductor Surfaces*. [Doctoral Thesis (compilation), Synchrotron Radiation Research]. Lund University (Media-Tryck).

Total number of authors:

1

General rights

Unless other specific re-use rights are stated the following general rights apply:

Copyright and moral rights for the publications made accessible in the public portal are retained by the authors and/or other copyright owners and it is a condition of accessing publications that users recognise and abide by the legal requirements associated with these rights.

- Users may download and print one copy of any publication from the public portal for the purpose of private study or research.
- You may not further distribute the material or use it for any profit-making activity or commercial gain
- You may freely distribute the URL identifying the publication in the public portal

Read more about Creative commons licenses: <https://creativecommons.org/licenses/>

Take down policy

If you believe that this document breaches copyright please contact us providing details, and we will remove access to the work immediately and investigate your claim.

LUND UNIVERSITY

PO Box 117
221 00 Lund
+46 46-222 00 00

Adventures of III-V Semiconductor Surfaces

SANDRA BENTER

DEPARTMENT OF PHYSICS | FACULTY OF SCIENCE | LUND UNIVERSITY



Adventures of III-V Semiconductor Surfaces

Sandra Benter



LUND
UNIVERSITY

DOCTORAL DISSERTATION

Doctoral dissertation for the degree of Doctor of Philosophy (PhD) at the Faculty of Science at Lund University to be publicly defended on 13th of October 2023 at 13.15 in Rydberg lecture Hall, Department of Physics

Faculty opponent

Charles Eddy, Science director of ONR and NRL

Organization: LUND UNIVERSITY

Document name: Doctoral thesis

Date of issue: 2023-10-13

Author(s): Sandra Benter

Sponsoring organization:

Title and subtitle: Adventures of III-V Semiconductor Surfaces

Abstract:

Tailoring the surface composition and morphology of materials to enable new electronic devices is important for a wide range of applications such as quantum computing or spintronics. A fundamental understanding of the changes induced in the surface during different process steps can help to establish new synthesis routes as well as devices. This thesis focuses on the manipulation of III-V semiconductor compounds, in particular the surfaces of InAs and GaAs crystals.

By implementing lithographically defined metal islands on the InAs surface, we push the boundaries of substrate annealing temperatures inhibiting the formation of In droplets locally. The employed Pd layer acts as a sink for freely diffusing In atoms above the congruent melting temperature. Here, As atoms go into gas phase at a higher rate compared to In due to the difference in vapor pressure. This lateral control over the concentration of In on the surface was investigated via scanning electron, atomic force as well as X-ray photoemission electron microscopy (XPEEM), and opens new pathways for epitaxy and the synthesis of heterostructures.

Furthermore, theoretical studies have shown that the implementation of Bi atoms into the lattice of III-V compound semiconductors can facilitate band gap reduction and increased spin-orbit coupling desirable for fabricating of topological insulators. Particularly, the interaction of group III elements with Bi has attracted great interest. However, manufacturing these diluted Bismides is not trivial, since most approaches like molecular beam epitaxy, synthesis from the melt or metal organic vapor deposition suffer from limited and inhomogeneous Bi incorporation into the crystal.

By following the approach of depositing Bi atoms onto a III-V sample and subsequent annealing, this thesis aims to synthesize and characterize heterostructures displaying III-V bulk properties and a surface made of III-As-Bi compounds. Different sample preparation routes were explored focusing on GaAs and InAs substrates with zinc blende (ZB) and wurtzite (WZ) crystal structure. The latter is only achievable in low-dimensional materials and will be employed in the form of InAs nanosheets. Part of this study focusses on the investigation of Bi-induced structural and chemical changes in the surface of the III-V compounds by utilizing surface sensitive techniques such as scanning tunneling microscopy, X-ray photoemission spectroscopy, low energy electron diffraction and XPEEM. Our results show that the mechanism of Bi incorporation is highly dependent on the underlying crystal structure, as well as process parameters such as time and substrate temperature.

Additionally, first band structure measurements of InAs WZ crystal nanosheets collected via averaging angle-resolved photoemission spectroscopy (ARPES) are presented. In contrast to other ZB crystal facets, a 2D electron gas (2DEG) is already detected after removing the native oxide and diminished after Bi deposition. We attribute the origin of the 2DEG to unique step and edge morphologies found on the WZ nanosheets. The thesis concludes with an ARPES study on InAs(111)B substrates presenting new electronic states inside the band gap based on the interaction of Bi and As atoms.

Key words: III-V, semiconductor, surface, InAs, GaAs, droplets, Bismuth, STM, XPS, ARPES, XPEEM

Classification system and/or index terms (if any)

Supplementary bibliographical information

Language English

ISSN and key title:

ISBN: 978-91-8039-753-7 (electronic)

978-91-8039-754-4 (printed)

Recipient's notes

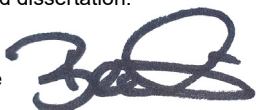
Number of pages:

Price

Security classification

I, the undersigned, being the copyright owner of the abstract of the above-mentioned dissertation, hereby grant to all reference sources permission to publish and disseminate the abstract of the above-mentioned dissertation.

Signature



Date 2023-08-28

Adventures of III-V Semiconductor Surfaces

Sandra Benter



LUND
UNIVERSITY

Front and back cover © Claudia Benter

Pages i-xiv, 1-81 © Sandra Benter

Paper 1 © Licensed under CC-BY 4.0 published by Springer Nature

Paper 2 © Licensed under CC-BY 4.0 published by American Chemical Society

Paper 3 © Licensed under CC-BY 3.0 published by Royal Society of Chemistry

Paper 4 © by the Authors (manuscript unpublished)

Paper 5 © by the Authors (manuscript unpublished)

Division of Synchrotron Radiation Research

Department of Physics, Faculty of Science

Lund University

ISBN 978-91-8039-753-7 (electronic)

978-91-8039-754-4 (printed)

Printed in Sweden by Media-Tryck, Lund University

Lund 2023



Media-Tryck is a Nordic Swan Ecolabel
certified provider of printed material.
Read more about our environmental
work at www.mediatryck.lu.se

MADE IN SWEDEN 

for all who care

Table of Contents

	Abstract	i
	Popular Science Abstract	iii
	Populärwissenschaftliche Zusammenfassung	vii
	List of Papers.....	x
	Abbreviations	xiii
1	How everything started.....	1
2	III-V semiconductors	5
	2.1 Crystal structure & surfaces	5
	Surface reconstruction	6
	2.2 Chemical environment.....	7
	2.3 Band structure.....	8
	2.4 Nanostructures	10
	Deposition method.....	11
3	Characterization Methods	15
	3.1 Scanning Tunneling Microscopy.....	15
	Short dive into the theory.....	16
	Employed scanning mode.....	17
	Imaging compounds.....	18
	Obstructions	19
	3.2 X-ray Photoemission Spectroscopy.....	21
	Measurement setup	22
	Soft X-rays.....	24
	Analysis of the spectra.....	24
	3.3 X-ray Photoemission Electron Microscopy.....	28
	Signals from elastically backscattered electrons.....	30
	3.4 Angle-resolved Photoemission Spectroscopy.....	32
	Accessing the perpendicular momentum	35
4	Sample manipulation	37
	4.1 Removing the native oxide.....	38
	Hydrogen treatment	38

	Oxide removal in an MBE system	41
4.2	Droplet formation	43
	Droplet mitigation.....	43
4.3	Manipulation via adatom deposition	48
	Structural changes.....	50
	Chemical fingerprint	58
	Electronic changes	63
5	Outlook.....	67
	References	70
	Acknowledgement.....	80

Abstract

Tailoring the surface composition and morphology of materials to enable new electronic devices is important for a wide range of applications such as quantum computing or spintronics. A fundamental understanding of the changes induced in the surface during different process steps can help to establish new synthesis routes as well as devices. This thesis focuses on the manipulation of III-V semiconductor compounds, in particular the surfaces of InAs and GaAs crystals.

By implementing lithographically defined metal islands on the InAs surface, we push the boundaries of substrate annealing temperatures inhibiting the formation of In droplets locally. The employed Pd layer acts as a sink for freely diffusing In atoms above the congruent melting temperature. Here, As atoms go into gas phase at a higher rate compared to In due to the difference in vapor pressure. This lateral control over the concentration of In on the surface was investigated via scanning electron, atomic force as well as X-ray photoemission electron microscopy (XPEEM), and opens new pathways for epitaxy and the synthesis of heterostructures.

Furthermore, theoretical studies have shown that the implementation of Bi atoms into the lattice of III-V compound semiconductors can facilitate band gap reduction and increased spin-orbit coupling desirable for fabricating of topological insulators. Particularly, the interaction of group III elements with Bi has attracted great interest. However, manufacturing these diluted Bismides is not trivial, since most approaches like molecular beam epitaxy, synthesis from the melt or metal organic vapor deposition suffer from limited and inhomogeneous Bi incorporation into the crystal.

By following the approach of depositing Bi atoms onto a III-V sample and subsequent annealing, this thesis aims to synthesize and characterize heterostructures displaying III-V bulk properties and a surface made of III-As-Bi compounds. Different sample preparation routes were explored focusing on GaAs and InAs substrates with zinc blende (ZB) and wurtzite (WZ) crystal structure. The latter is only achievable in low-dimensional materials and will be employed in the

form of InAs nanosheets. Part of this study focusses on the investigation of Bi-induced structural and chemical changes in the surface of the III-V compounds by utilizing surface sensitive techniques such as scanning tunneling microscopy, X-ray photoemission spectroscopy, low energy electron diffraction and XPEEM. Our results show that the mechanism of Bi incorporation is highly dependent on the underlying crystal structure, as well as process parameters such as time and substrate temperature.

Additionally, first band structure measurements of InAs WZ crystal nanosheets collected via averaging angle-resolved photoemission spectroscopy (ARPES) are presented. In contrast to other ZB crystal facets, a 2D electron gas (2DEG) is already detected after removing the native oxide and diminished after Bi deposition. We attribute the origin of the 2DEG to unique step and edge morphologies found on the WZ nanosheets. The thesis concludes with an ARPES study on InAs(111)B substrates presenting new electronic states inside the band gap based on the interaction of Bi and As atoms.

Popular Science Abstract

Surfaces - one thing we are in contact with all day, every day. Understanding how surfaces influence the performance and application of electronic devices is not trivial. So, let's take a step back. Imagine you have a small plot of land and would like to grow tomatoes – the small, red ones full of sweet flavor. Luckily, you managed to get a bunch of seeds from a friend. However, your gardening experience is very limited and you decide to start by plowing the whole area to remove any unwanted weeds.

In contrast to tomato plants, I investigated the surface of Indium Arsenide (InAs) and Gallium Arsenide (GaAs) in the presented thesis. InAs and GaAs are two compound materials commonly employed in light emitting diodes (LEDs), transistors and infrared sensors due on their semiconductive character. Instead of plowing, I used atomic Hydrogen together with an increased sample temperature to remove contamination on the surface. Subsequently, various fabrication procedures were analyzed to understand which yields the desired outcome: a change in the electronic properties of the raw material. All experiments were carried out in ultra-high vacuum. Therefore, the samples were introduced into a specific chamber system which was subsequently evacuated from most molecules normally found in the atmosphere. As these molecules usually interact with the sample, the established vacuum enabled unchanged surfaces for our measurements.

The first study presented in this thesis focuses on the behavior of InAs samples during high temperature annealing steps. Here, the sample temperature was increased until enough energy is supplied for one element to leave the surface. For temperatures around 500-650°C, this is Arsenic. As a result, an excess of In atoms is present on the surface eventually forming droplets. This effect is undesirable for a lot of fabrication processes. Similarly, heavy rain fall in your garden can hinder you to plant and take care of your plants. If the soil is oversaturated with water, puddles will form, maybe even a small pond. Here, a drainage system could help to remove all the water despite the occasional heavy rain. A comparable approach was implemented on the InAs surfaces. With the help of metal contacts, the excess In atoms could be redirected into the metal and a droplet free area was established. We found that the effect is time and temperature dependent. Additionally, the

composition of the metal contacts is crucial, since it will determine how many free In atoms can be removed.

In your garden, you come up with an idea to make sure that you harvest at least some tomatoes. Therefore, you divide the ground into several testing areas. For each you adapt your gardening approach in a slightly different way: some seeds are planted in Dezember and others in May, some are watered and fed with fertilizer, and some are left for the weather to be cared by. The following studies in my thesis could be described in a similar way. Here, Bismuth (Bi) atoms were ‘planted’ into the surface of InAs and GaAs substrates via atomic deposition. For some samples, the temperature was left at room temperature during this treatment and for others it was raised to about 300°C. All samples were subsequently heated (also called annealed) to around 400°C. To gain a deeper understanding of the induced changes appearing after each treatment step, surface sensitive measurement techniques were employed. First, structural measurements were carried out which enabled us to understand the arrangement of the atoms within the surface. In a gardening setup, this is comparable to analyzing the overall growth of your tomato plants. Did they grow in an ordered fashion along a certain line, or did a couple of plants rooted intertwined within the same small area? As, this investigation occupied you for a while, it is now time to harvest.

To your surprise there are actual tomatoes to be gathered and you can not only collect red ones, but also yellow and purple tomatoes grew. Based on the record you kept during the year about the seed shape and gardening procedures, you understand that your friend provided you with different tomato plants and their shape and size correlates to your care. Similarly, an investigation of the chemical state of the InAs and GaAs samples allows for an understanding of other properties like the overall morphology (structure) of the surface or electronic characteristics. In general, the structural and chemical properties varied for the InAs and GaAs depending on the underlying atomic arrangement, deposition procedure and subsequent annealing temperature. A range from ordered incorporation on the atomic scale to cluster formation on the surface was observed. Additionally, Bi atoms favored bonding to one substrate element more compared to the other with respect to the sample temperature, e.g. bonding with In atoms on InAs surfaces for higher temperatures. Based on these results, the final studies in this thesis focus on the electronic characterization of InAs samples.

These electronic characterizations are also the last step of your gardening experience. The growth of the plants, the appearance and smell of the harvested tomatoes might give you a hint of their taste. However, you only know for certain whether the flavor was worth the hustle until you tried some... Well, it might not be the sweet flavor you hoped for, but instead it is complex and fruity. Likewise, the electronic properties observed and described in the last two studies for InAs samples interacting with Bi are unexpected but every bit as interesting.

Since a lot of work has gone into structural and chemical analysis, this thesis can only provide a glimpse of the potential of Bi intertwined with InAs or GaAs for future electronic devices. However, it provides a road map towards further investigations by linking different process parameters to observed atomic arrangement and chemical environment of each surface.

Populärwissenschaftliche Zusammenfassung

Oberflächen – etwas womit wir tagtäglich in Berührung sind. Es ist jedoch nicht ganz einfach den Einfluss von Oberflächen auf die Leistung und Anwendung von elektronischen Bauteilen zu verstehen. Lass uns also einen Schritt zurücktreten. Stell dir vor, du hast ein kleines Stückchen Land und würdest gerne Tomaten anbauen – die kleinen, roten mit dem süßen Geschmack. Dafür hast du dir ein paar Samen besorgt. Noch ist dein Erfahrungsschatz beim Gärtnern gering und du entscheidest dich als erstes die gesamte Fläche um zu pflügen, um unerwünschtes Unkraut zu entfernen.

Im Gegensatz zu Toamtenpflanzen habe ich in der hier präsentierten Arbeit die Oberfläche von Indiumarsenid (InAs) und Galliumarsenid (GaAs) untersucht. InAs und GaAs sind zwei Verbundmaterialien, die aufgrund ihres halbleitenden Eigenschaften häufig in Leuchtdioden (LEDs), Transistoren und Infrarotsensoren verwendet werden. Anstelle des Pflügens habe ich atomaren Wasserstoff zusammen mit einer erhöhten Proben temperatur genutzt, um Verunreinigungen auf der Oberfläche zu entfernen. Anschließend wurden verschiedene Fertigungsverfahren analysiert, um zu verstehen, welches das gewünschte Ergebnis bringt: eine Veränderung der elektronischen Eigenschaften des Rohmaterials. Alle Experimente wurden im Ultrahochvakuum durchgeführt. Dazu wurden die Proben in ein spezielles Kammernsystem eingebracht, aus der anschließend die meisten in der Atmosphäre befindlichen Moleküle rausgepumpt wurden. Da diese Moleküle normalerweise mit der Probe in Wechselwirkung treten, ermöglichte das hergestellte Vakuum die Analyse und Messung unveränderte Oberflächen.

Die erste Studie befasst sich mit dem Verhalten von InAs-Proben bei hohen Proben temperatur. Dabei wird diese so lange erhöht, bis genügend Energie zugeführt wird, so dass ein Element die Oberfläche verlässt. Bei Temperaturen von 500-650°C ist dies Arsen. Infolgedessen befindet sich ein Überschuss an In-Atomen auf der Oberfläche und bildet Tröpfchen. Dieser Effekt ist für viele Herstellungsprozesse unerwünscht. In ähnlicher Weise kann starker Regen in deinem Garten dich beim Pflanzen und Pflegen deiner Pflanzen behindern. Wenn

der Boden mit Wasser übersättigt ist, bilden sich Pfützen, vielleicht sogar ein kleiner Teich. Hier könnte ein Drainagesystem helfen, das gesamte Wasser trotz gelegentlicher starker Regenfälle abzuführen. Ein vergleichbarer Ansatz wurde bei den InAs-Oberflächen umgesetzt. Mit Hilfe von Metallkontakten konnten die überschüssigen In-Atome in das Metall umgelenkt werden, und es entstand ein tropfenfreier Bereich. Dieser Effekt ist zeit- und temperaturabhängig. Außerdem bestimmt die Zusammensetzung der Metallkontakte maßgeblich, wie viele freie In-Atome entfernt werden können.

Um sicherzustellen, dass du in deinem Garten zumindest einige Tomaten ernten wirst, hast du eine Idee. Dafür unterteilst du den Boden in mehrere Versuchsflächen. Für jede dieser Flächen passt du dein gärtnerisches Vorgehen ein wenig an: einige Samen werden im Dezember und andere im Mai gepflanzt, einige werden bewässert und gedüngt, und einige überlässt du dem Wetter. Die folgenden Studien in meiner Arbeit könnten auf ähnliche Weise beschrieben werden. Hier wurden Bismut (Bi)-Atome durch atomares Aufdampfen in die Oberfläche von InAs- und GaAs-Substraten "gepflanzt". Bei einigen Proben wurde die Temperatur während dieses Prozesses bei Raumtemperatur belassen, bei anderen wurde sie auf etwa 300 °C erhöht. Alle Substrate wurden anschließend auf ca. 400 °C erhitzt. Oberflächensensitive Messtechniken wurden eingesetzt, um ein besseres Verständnis über die Vorgänge im Material nach jedem Prozessschritt zu erlangen. Zunächst wurden Strukturmessungen durchgeführt, die es ermöglichen, die Anordnung der Atome innerhalb der Oberfläche zu verstehen. Im Gartenbau ist dies vergleichbar mit der Analyse des Gesamtwachstums deiner Tomatenpflanzen. Sind sie in geordneter Weise entlang einer bestimmten Linie gewachsen, oder wurzelten ein paar Pflanzen ineinander verschlungen auf der gleichen kleinen Fläche? Da diese Untersuchungen dich länger beschäftigt haben, ist es inzwischen Erntezeit geworden.

Zu deiner Überraschung sind tatsächlich Tomaten gewachsen, und du kannst nicht nur rote, sondern auch gelbe und violette Tomaten ernten. Anhand der Aufzeichnungen, die du im Laufe des Jahres über die Form der Samen und die Anbaumethoden geführt hast, verstehst du, dass du verschiedene Tomatenpflanzen ausgesät hast und dass deren Form und Größe mit deiner Pflege zusammenhängt. In ähnlicher Weise ermöglicht die Untersuchung des chemischen Zustands der InAs- und GaAs-Proben ein Verständnis anderer Eigenschaften wie der

Oberflächenstruktur oder der elektronischen Merkmale. Im Allgemeinen verändert das Aufdampfen und die folgenden Prozessschritte die Oberfläche von InAs und GaAs. Die gemessenen strukturellen und chemischen Eigenschaften sind dabei von der zugrunde liegenden Kristallstruktur, dem Bedampfungsverfahren und der anschließenden Aufheiztemperatur der Probe abhängig. Von geordneten atomaren Strukturen bis hin zur Clusterbildung war alles vertreten. Darüber hinaus bevorzugten Bi-Atome in Abhängigkeit von der Probertemperatur die Bindung zu einem speziellen Substratelement, z. B. die Bindung mit In-Atomen in InAs-Oberflächen bei höheren Temperaturen. Auf der Grundlage dieser Ergebnisse konzentrieren sich die abschließenden Untersuchungen in dieser Arbeit auf die elektronische Charakterisierung von InAs-Proben.

Diese elektronische Charakterisierung ist der letzte Schritt deiner Gartenerfahrung. Das Wachstum der Pflanzen, das Aussehen und der Geruch der geernteten Tomaten können dir vielleicht einen Hinweis auf ihren Geschmack geben. Ob sich die Mühe gelohnt hat, weiß man aber erst, wenn man sie probiert hat... Nun, sie schmecken vielleicht nicht so süß wie erhofft, dafür aber komplex und fruchtig. In ähnlicher Weise sind die elektronischen Eigenschaften, die in den letzten beiden Studien für InAs-Proben in Wechselwirkung mit Bi beobachtet und beschrieben wurden, unerwartet, aber nicht minder interessant.

Da viel Arbeit in die strukturelle und chemische Analyse der Proben geflossen ist, kann diese Arbeit nur einen kleinen Einblick in das Potenzial von Bi in Verbindung mit InAs oder GaAs für künftige elektronische Geräte geben. Sie liefert jedoch einen Fahrplan für weitere Experimente, indem verschiedene Prozessparameter mit der beobachteten atomaren Anordnung und der chemischen Umgebung der jeweiligen Oberfläche verknüpft sind.

List of Papers

This thesis is based on the following papers, referred in the text by their roman numerals.

I. Geometric control of diffusing elements on InAs semiconductor surfaces via metal contacts

Sandra Benter, Adam Jönsson, Jonas Johansson, Lin Zhu, Evangelos Golias, Lars-Erik Wernersson and Anders Mikkelsen

Nature Communications 2023, **14**, 4541

I prepared part of the samples, applied for the beamtime, planned the experiments, carried out the data acquisition and analysis (for AFM, SEM and XPEEM measurements), and was main responsible for the manuscript.

II. A 2D Bismuth-Induced Honeycomb Surface Structure on GaAs(111)

Yi Liu, Sandra Benter, Chin Shen Ong, Renan P. Maciel, Linnéa Björk, Austin Irish, Olle Eriksson, Anders Mikkelsen, and Rainer Timm

ACS Nano 2023, **17**, 5047–5058

I took part in the XPS experiments, discussion for data analysis and gave feedback on the manuscript.

III. Tuneable 2D surface Bismuth incorporation on InAs nanosheets

Sandra Benter, Yi Liu, Renan Da Paixao Maciel, Chin Shen Ong, Lassi Linnala, Dong Pan, Austin Irish, Yen-Po Liu, Jianhua Zhao, Hongqi Xu, Olle Eriksson, Rainer Timm and Anders Mikkelsen

Nanoscale, 2023, **15**, 9551-9559

I designed the XPS experiments, applied for beamtime, carried out the data acquisition and analysis, and was main responsible for the manuscript.

IV. Electron accumulation on InAs Wurtzite nanosheet surfaces

Sandra Benter, Marco Bianchi, Dong Pan, Jianhua Zhao, Hongqi Xu, Philip Hofmann and Anders Mikkelsen

In manuscript

I designed the ARPES and XPS experiments, applied for beamtime, carried out the data acquisition and analysis, and was main responsible for the manuscript.

V. Bismuth-Arsenic surface structure on InAs(111)B

Sandra Benter, Renan Da Paixao Maciel, Sébastien Plissard, Chin Shen Ong, Olle Eriksson, Rainer Timm and Anders Mikkelsen

In manuscript

I established the collaboration for sample preparation, designed the experiment, carried out the ARPES and XPS data acquisition and analysis, and was main responsible for the manuscript.

Publications to which I have contributed but are not included in this thesis.

Quasi One-Dimensional Metal–Semiconductor Heterostructures

S. Benter, V. G. Dubrovskii, M. Bartmann, A. Campo, I. Zardo, M. Sistani, M. Stöger-Pollach, S. Lancaster, H. Detz, and A. Lugstein

Nano Letters 2019, **19**, 3892–3897

I prepared the samples, carried out the SEM data acquisition and analysis, and wrote the first draft.

Tuning oxygen vacancies and resistive switching properties in ultra-thin HfO₂ RRAM via TiN bottom electrode and interface engineering

Zhihua Yong, Karl-Magnus Persson, Mamidala Saketh Ram, Giulio D’Acunto, Yi Liu, Sandra Benter, Jisheng Pan, Zheshen Li, Mattias Borg, Anders Mikkelsen, Lars-Erik Wernersson and Rainer Timm

Applied Surface Science 2021, **551**, 149386

I took part in the XPS experiments.

Inducing ferroelastic domains in single-crystal CsPbBr₃ perovskite nanowires using atomic force microscopy

Lucas A. B. Marçal, Sandra Benter, Austin Irish, Dmitry Dzhigaev, Eitan Oksenberg, Amnon Rothman, Ella Sanders, Susanna Hammarberg, Zhaojun Zhang, Simone Sala, Alexander Björling, Eva Unger, Anders Mikkelsen, Ernesto Joselevich, Rainer Timm, and Jesper Wallentin

Physical Review Materials 2021, **5**, L063001

I carried out the AFM measurements, took part in the discussion of the results and wrote the section regarding these measurements in the manuscript.

Abbreviations

ARPES	angle-resolved photoemission spectroscopy
CB	conduction band
DFT	density functional theory
DFZ	droplet-free zone
EA	electron analyzer
fcc	face-centered cubic
(L)DOS	(local) density of states
LEED	low energy electron diffraction
LEEM	low energy electron mode
MBE	molecular beam epitaxy
MEM	mirror electron mode
ML	monolayer
MOVPE	metal organic vapor-phase epitaxy
SEM	scanning electron microscopy
SPELEEM	spectroscopic photoelectron and low energy electron microscope
STM	scanning tunneling microscopy
RT	room temperature
UHV	ultra-high vacuum
VB	valence band
WZ	wurtzite
XPEEM	X-ray photoelectron emission microscopy
XP(S)	X-ray photoelectron (spectroscopy)
ZB	zinc blende
2DEG	2D electron gas

1 How everything started

This is a story about small things; about defeat, perseverance and unexpected science. But let's start from the beginning.

After the advent of semiconductor devices¹⁻⁴ based on a single element like Si or Ge, the search for other materials exhibiting similar or superior characteristics began in the 1950s^{5,6} by looking into elements with similar atomic numbers. As a natural result, compounds consisting of elements from group III and V in the periodic table gained high interest in the research community. Very soon, first studies about electronic characteristics of, e.g. GaAs^{7,8}, InAs⁹⁻¹¹ and InSb^{8,12-14} were published.

Nowadays, III-V semiconductor compounds are core elements in our daily life in form of light emitting diodes (also known as LEDs) for decoration and illumination, optical sensors for infra-red light, or transistors in our mobile phones, cars and other electronics to only name a few applications. Although the lion's share of our electronic devices is still Si-based, III-V semiconductors are capable of outperforming Si-technology in the mentioned areas due to their direct band gap, high carrier mobility and low power dissipation^{5,15-17}. Therefore, III-V semiconductors have sparked great interest and promise to help facilitate the next generation of electric devices such as quantum computing and spintronics.

As a result of the continuous down-scaling of electronics described by Moore's law¹⁸, the importance of bulk properties started to compete with characteristics induced by the surface. Devices with side lengths down to sub-nanometers^{19,20} exhibit (almost) exclusively atoms positioned at the surface. Moreover, their fabrication always involves the growth of different materials on top of each other, e.g., in form of deposition or epitaxial synthesis. Consequently, the substrate surface is a key element for the subsequent device quality and performance. Therefore, it is essential to investigate and understand surface induced phenomena.

It is at this crossroad that the work presented in this thesis is situated. The purpose of the journey described below is to advance the capabilities of III-V semiconductor

compounds by establishing and investigating a growth-synthesis-function relationship targeted at the surfaces of these materials. This bridge will interconnect structural information on the atomic scale with understanding of favored bond formation. Subsequently, a glimpse of potential electronic properties will be given.

For III-V compounds, there are two main surface manipulation routes: changing the surface by (i) changing the concentration of an element already present, or (ii) introducing a new one. Moving along path (i), the stoichiometry of the compound as well as the crystal surface structure can be varied already during the growth (typically also affecting the bulk) via sample temperature and different flux ratios of the precursors, or subsequently by, e.g. annealing. As a result, carrier concentrations and mobilities can be tuned²¹, as well as different surface reconstruction realized^{22,23}. However, III-V compounds can suffer from cluster formation on the surface. This can occur due to an increased flux of a single element during growth^{24–26} or by choosing annealing temperatures above the congruent melting temperature. Here, one element (usually based in group V) is more volatile compared to the other and goes into gas phase at a much higher rate. This leads to an excess of group III elements and is commonly observed for heat treatments without any backpressure^{27–29}. This effect degrades the quality of the surface due to its increased roughness based on droplet formation and surface vacancies. Thus, it limits the mobility of charge carriers³⁰ and quality of epitaxial growth on top³¹. In **paper I**, we investigate how lithographically defined metal stacks can inhibit the formation of droplets on an InAs surface and allow for higher sample temperatures without immediate surface degradation. The described phenomena can push the boundaries of common device fabrication processes and allow for the investigation of before inaccessible fabrication parameters.

Taking path (ii) typically increases the complexity of the III-V compound semiconductors regarding the atomic and chemical structure. In principle, any new element introduced into the crystal lattice will affect its electronic properties at least via doping or introducing lattice defects. However, by limiting the selection to group III and V elements, the substitution of original lattice atoms is easier allowing to maintain an overall ordered crystal structure. These compounds are called ternary III-V materials and consist of either two group III and one group V element or vice versa. Introducing a third element into the semiconductor crystal is very interesting

for opto-electronic devices, since it allows for concentration dependent manipulation of the band gap^{32–34} (as can be seen in figure 1.1) and of the effective mass of charge carriers³⁵. Furthermore, by implementing Bi (group V element) into III-V lattices spin-orbit splitting can potentially be increased, effectively enhancing the lifetime of excitons³³. The induced lattice mismatch strengthens localization effects on excitons additionally³⁶. These characteristics are desirable for certain electronic materials such as topological insulators, where metallic edge states are present in the surface and the bulk material displays a band gap.

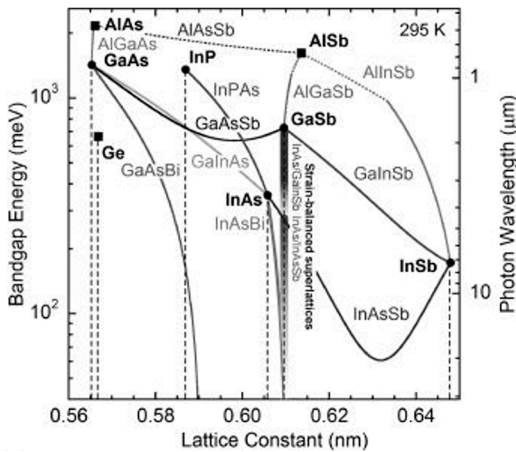


Figure 1.1 Band gap energy as a function of the lattice constant for selected III-V binary and ternary alloys with the lattice constants of common substrates indicated with vertical dashed lines for room temperature. Reproduced with permission from AIP Publishing from ³⁷.

There are several methods to grow and manipulate ternary III-V systems and subsequently their surfaces. However, most of them involve rather complex equipment. In general, synthesis from the melt often suffers from crack formation and alloy segregation¹ in the material³⁸. Here, no new raw material can be introduced during the growth to counteract this problem reducing the obtainable surface quality dramatically. Additionally, no clear difference in atomic arrangement or elemental concentration between the bulk and surface can be achieved. On the other hand, epitaxial growth of materials onto a substrate allows for a direct manipulation of the surface during synthesis by varying the flux of gaseous precursors, e.g., in molecular beam epitaxy (MBE) or metal organic vapor-

¹ Since one element will be slower incorporated leading to a liquid phase enriched with this element, the result is a concentration gradient within the bulk.

phase epitaxy (MOVPE). These techniques might offer a higher control over the Bi:III:V flux ratio and sample temperature during the growth but do not manage to overcome the miscibility gap limiting the amount of Bi that can be incorporated. In general, films with inhomogeneous concentration distribution and low Bi incorporation are often the result³⁹. Furthermore, studies show that the ability to form a ternary compound is crystal facet dependent^{40,41}. Up to now a maximum of ~22% Bi incorporation was achieved on GaAs⁴² and 6.4% on InAs(100)³⁷ surfaces.

Studies of our group have demonstrated that ternary III-V based systems can be implemented in a very simple manner. By evaporating the desired element onto the III-V substrate and additional heat treatment, it was shown that Sb and Bi atoms start to substitute As atoms within the surface lattice of GaAs nanostructures with different crystal facets^{43,44}. The fabrication of heterostructures with Bi atoms in the top layer and atomically sharp interfaces is facilitated. Based on this approach, **paper II, III and V** further investigate the Bi incorporation into various InAs and GaAs crystal facets of bulk and low-dimensional specimen by linking structural, chemical, and electronic observations with theoretical calculations.

To understand the changes induced by the adatom substitution, knowledge of the pristine substrate is essential. **Paper IV** presents experimental data for the band structure of InAs samples with a wurtzite crystal structure only growable in low dimensional materials.

In the following chapters, the protagonists of the upcoming endeavours will be introduced, and their main properties highlighted. They will encounter various characterization techniques whose basic working principle will be presented shortly thereafter. The main part of the book will focus on the adventures of the III-V surfaces inside a vacuum cave system. Here, they must face the challenges of surface alteration and in-depth investigation. The key findings of **paper I-V** will be emphasized and accompanied with additional structural results. In the end, a prediction of future adventures will be given.

2 III-V semiconductors

This chapter will introduce the heroines of the following stories. It will give an overview of important characteristics and form of appearances both applicable to InAs and GaAs crystals. Further, the InAs nanostructures highlighted in **paper III** and **IV** are introduced and two deposition techniques illustrated.

2.1 Crystal structure & surfaces

As one might have already guessed, the main character of the upcoming adventures is InAs. Here and there, its sibling GaAs will also have some appearances. InAs (like GaAs) is a compound semiconductor material, which crystallizes in a zinc blende (ZB) structure when grown in bulk. As advances of growth processes in the early 2000s enabled the fabrication of low dimensional materials, compound semiconductors with a wurtzite (WZ) crystal structure became available. While ZB is based on two face-centered cubic (fcc) lattices shifted by $\frac{1}{4}$ of the unit cell with respect to each other, WZ is a hexagonal Bravais lattice. This amounts to a difference in the stacking sequence as indicated for the WZ $(11\bar{2}0)$ (ABAB...) and ZB (110) (ABCA...) surfaces in top view in figure 2.1.

Cutting along certain planes allows for a variety of configurations regarding atomic arrangement, lattice constant and elements present on the surface. Here, we will focus on three surfaces: (i) $(11\bar{2}0)$ – a non-polar WZ surface with atomic armchair arrangement, (ii) (110) – also a non-polar ZB crystal surface with atomic zick-zack arrangement, and (iii) $(111)B$ – a polar ZB crystal surface with hexagonal arrangement where solely As atoms exhibit dangling bonds in the case of InAs and GaAs². All substrate types are depicted in figure 2.1. Interestingly, the WZ $(11\bar{2}0)$

² Turning the crystal upside down will expose the $(111)A$ facet at the top, solely exhibiting dangling bonds for In or Ga atoms for InAs and GaAs crystals, respectively.

and ZB (110) surface exhibit the same nearest neighbor configuration indicated by the shadowed area.

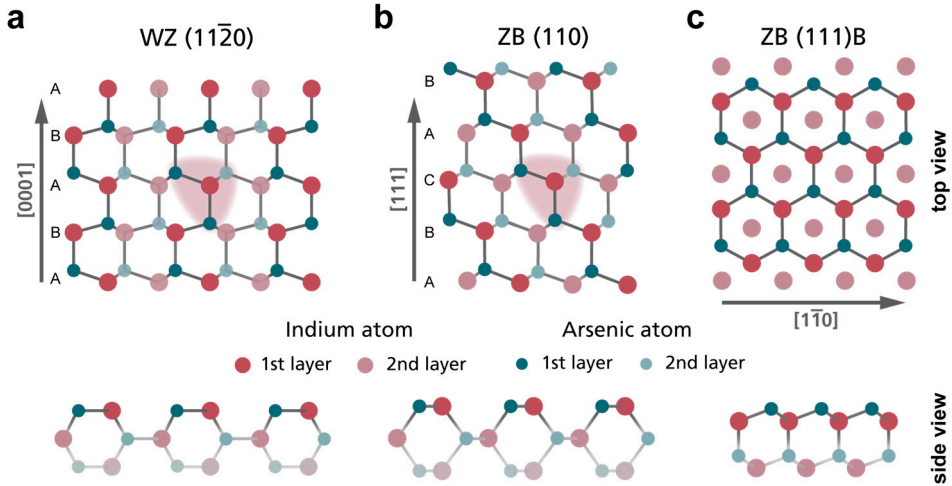


Figure 2.1 Ball model of InAs with a WZ (11 $\bar{2}$ 0) (a), ZB (110) (b), and ZB (111)B crystal facet in top view (upper) and side view (bottom). The different stacking sequence of the WZ and ZB crystal is indicated with capital letters. Note, the surface in (a) and (b) exhibit the same nearest neighbor configuration indicated by the shadowed area independent of the crystal structure.

Surface reconstruction

By creating a surface, the symmetry of the bulk is broken. As a result, surface atoms might shift away from the ideal lattice position to decrease the number of dangling bonds and minimize the total energy of the surface. There are two types of surface rearrangement: (i) relaxation and (ii) reconstruction. For (i), the distance between the top and second layer decreases with respect to the interlayer distance in the bulk. In the case of (ii), the surface atoms rearrange in a 2D manner with respect to the bulk position as depicted in figure 2.2a. Here, surface atoms were removed to reduce the total energy of the surface as far as possible. Surface reconstruction is a phenomenon often observed on InAs or GaAs substrates for different sample preparation processes^{22,45–53}. An example of an InAs(111)A surface with a (2x2) reconstruction based on the results of⁵⁰ is displayed in figure 2.2b. Interestingly,

reconstruction can also occur due to the absorption of adatoms different from the substrate. In this case, the presence of a new element changes the interatomic forces and results in rearrangement of the surface as detected for InAs(110) with Bi⁵⁴, or Sb on GaAs(001)⁵⁵. To define the surface reconstruction with respect to the original unit cell, the Wood's and Matrix notation can be used, see figure 2.2.

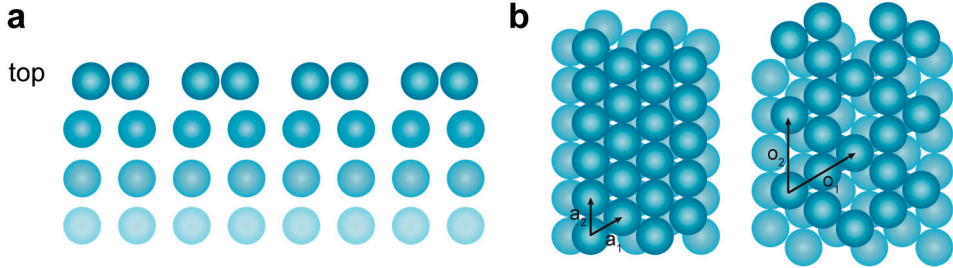


Figure 2.2 (a) Ball model of a surface reconstruction in cross-sectional view. (b) Ball model in top view of an InAs(111)A surface with a (1x1) (left) and a (2x2) in Wood's or a $\begin{pmatrix} 2 & 0 \\ 0 & 2 \end{pmatrix}$ in Matrix notation (right) reconstruction based on the observations of⁵⁰.

As the crystal phase influences the outer appearance and form of our protagonist, it also determines the inner characteristics important for the type of adventures the material will be involved in. In the following, I will shortly introduce two properties that are unique to our material similar to a fingerprint for a person.

2.2 Chemical environment

Since InAs and GaAs are compound semiconductors, two elements are required to build their respective crystal lattice. Both are evenly distributed as can be seen in figure 2.1 with one As atom bonding to four In (or Ga) atoms and vice versa in a convolution of covalent and ionic bonding⁵⁶. Due to the higher electron negativity of As, it will attract electrons from the respective bonding partners. As a result, core electrons of the As orbitals will experience less attraction towards the nucleus and be more loosely bound compared to electrons from the same orbital in a single As atom in gas phase. In contrast, core electrons of the In or Ga will shift slightly closer

towards the nucleus. These changes in binding energy can be detected with X-ray photoelectron spectroscopy (XPS - a short introduction to the technique can be found in section 3.2). The XPS spectra of the As 3d and In 4d core level of an InAs wafer piece after removing the native oxide are shown in figure 2.3. For the displayed ZB (110) crystal, In and As atoms are present at the surface in equal parts. Interestingly, differences arising in the binding energy of the surface and bulk atoms can be detected. This is a result of the dangling and unsatisfied bonds of the surface atoms.

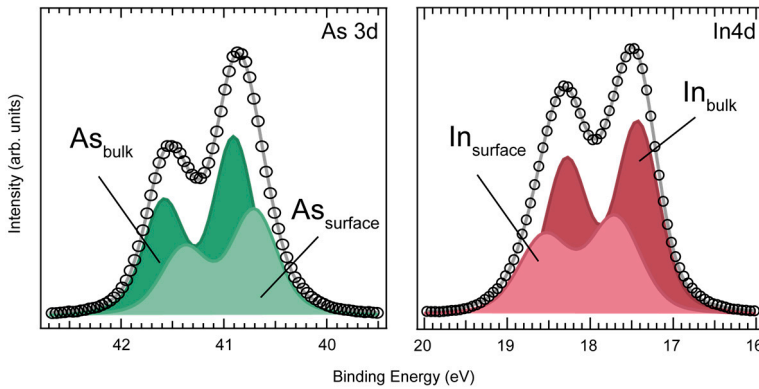


Figure 2.3 XP core level spectra of As 3d (left) and In 4d (right) of a InAs(110) surface after removing the native oxide. Noteworthy, the surface component is at lower/higher binding energy in comparison to the bulk component, respectively.

2.3 Band structure

As a result of the atomic arrangement within the semiconductor crystal, electron energy levels of adjacent atoms start to overlap. Subsequently, the discrete energy level splits into numerous levels depending on the number of interacting atoms. For a solid, this is in the range of 10^{22} . Due to the very close spacing between these energy states, an energy band is formed. This is mostly applicable for the outer most energy levels of an atom contributing to the electric conductivity. For semiconductors, such as InAs and GaAs, a band gap between the highest occupied, so-called valence band (VB), and lowest unoccupied band, so-called conduction band (CB), is present. It is important to note that the position of the maximum of

the VB coincides with the minimum of the CB for InAs and GaAs. Both have therefore a direct band gap interesting for opto-electronic applications^{57–60}. Focusing on InAs, one might anticipate that the band structure for ZB and WZ crystals is different. Figure 2.4 shows the theoretical calculations for ZB and WZ InAs crystals. Both exhibit a direct band gap at the Γ -point^{61,62}. Noteworthy, on average there are more energy levels available below the Fermi level at each symmetry point for the WZ crystal in figure 2.4. It should be pointed out that E_F is typically assumed to be at the VB maximum for calculated band structures. This deviates from the position of the Fermi level in experimental spectroscopy data as will be shown in chapter 3.

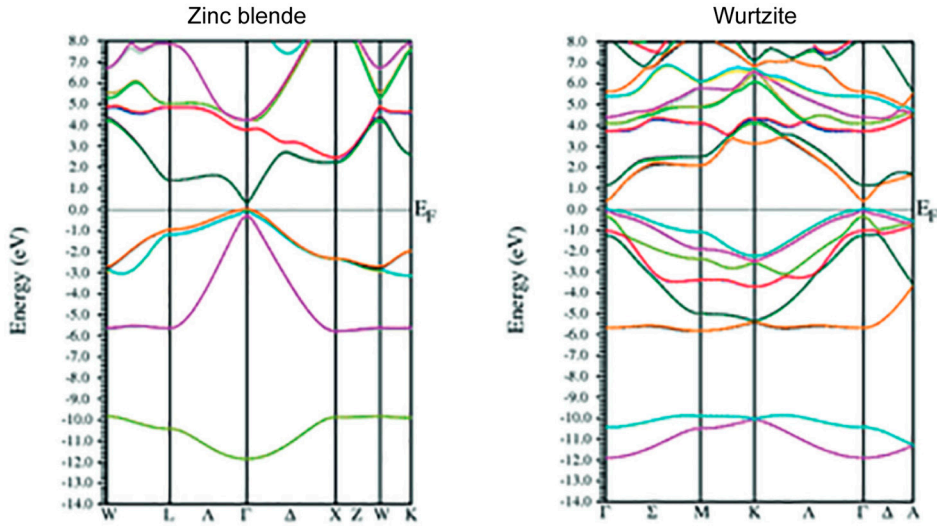


Figure 2.4 Band structure of an InAs sample with ZB (left) and WZ (right) crystal structure. Reproduced with permission from SAGE Publications from⁶¹.

As for now, the band structure of ZB InAs crystals found in bulk have been experimentally studied to a large extent via angle-resolved photoemission spectroscopy^{63–66} (ARPES – a short introduction to the technique can be found in section 3.4). However, resolving the WZ crystal structure is rather challenging due to the nanometer size and shape of the necessary specimen. In section 4.3 and **paper IV**, we demonstrate that under certain conditions the band structure of InAs

nanosheets exhibiting WZ (11 $\bar{2}$ 0) can be explored experimentally without the requirement of focusing on a single specimen.

2.4 Nanostructures

As the quests of the III-V semiconductor compounds might call for a variety of characteristics, InAs and GaAs have demonstrated to accommodate a multitude of different shapes and facets when grown in low dimensional material. Generally, two different routes can be explored when manufacturing nanostructures: bottom-up or top-down. All protagonists on the nm- and μm scale participating in this book have been grown bottom-up in an MBE system. Here, commonly a metallic catalyst, e.g. Au or Ag, is deposited onto a growth substrate in the form of particles or droplets. At the desired process temperature, the sample is exposed to a gas flux of the desired group III and V element, in our case In and As. The overall growth mechanism is very intricate⁶⁷, but is usually generalized to: the desired synthesis elements will oversaturate within the metallic catalyst enabling the deposition of III-V layers at the interface to the substrate. By varying the ratio between the two fluxes a variety of specimen with different appearances can be grown ranging from nanowire to nanosheet, with or without tree-like branching⁶⁸, where the growth in vertical direction is governed by vapor-solid-solid and in the lateral by vapor-liquid-solid growth. The resulting forest of nanostructures for a growth temperature of 525°C inhibiting branching significantly, as well as the resulting variety in shapes are depicted in figure 2.5.

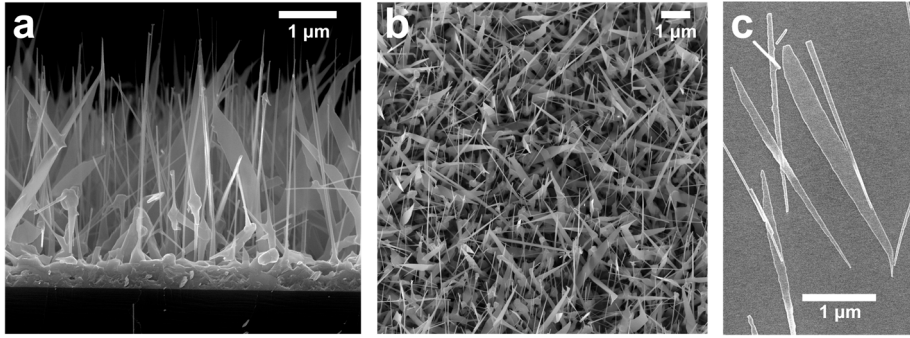


Figure 2.5 (a) cross-sectional and (b) top view of InAs nanosheets grown at 525°C. Image courtesy of Dong Pan (Institute of Semiconductors, Chinese Academy of Sciences, Beijing). (c) Top view of InAs nanosheets after deposition onto the measurement sample.

A variety of methods is available to fabricate low dimensional III-V based compounds (like aerosol epitaxy or metal organic chemical vapor deposition). I will not expand on these, since the specimen used in **paper III** and **IV** were fabricated via MBE as shortly discussed above. To be more precise, one of the main characters in this book are InAs nanosheets as depicted in figure 2.5 and 2.7. Their main crystal facet is WZ ($11\bar{2}0$) intermitted by single monolayers of ZB (110). Their dimensions range from 100-500 nm wide and 1-2 μm long with a thickness of about 20 nm and are therefore quasi 2D.

Deposition method

As can be seen from figure 2.5, the density of nanostructures on the growth substrate is high. Due to the employed synthesis technique, their main facet is not oriented upwards and instead pointing to the side. This imposes some difficulties when the key element of the study is surface manipulation and characterization. Therefore, it is more favorable to transport some nanosheets on to other surfaces. A schematic of the contact transfer method is depicted in figure 2.6a, in which the measurement sample is placed upside down on top of the growth sample. By applying a directional force downwards and towards the sample edge, the nanometer sized specimen will be broken off and deposited on to the desired surface. With some training a gradient

of nanostructures can be accomplished in which the respective area density is suitable for different analyzing techniques as indicated in figure 2.6b.

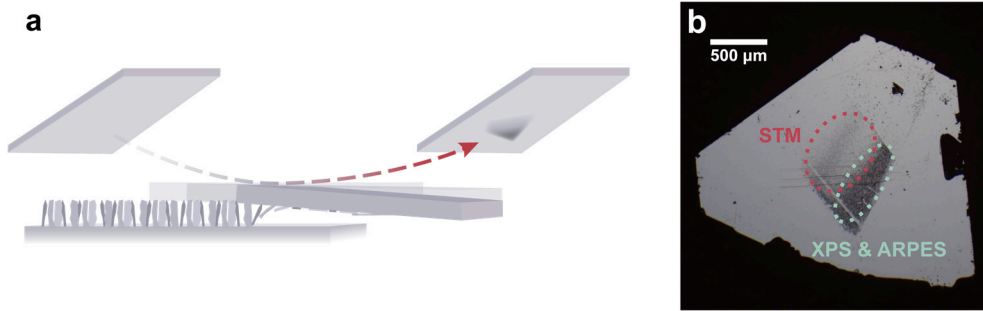


Figure 2.6 (a) Schematic of the contact transfer method used to transfer a high density of nanostructures. The shadowed area on the right surface (indicated by the red arrow) depicts the deposition gradient accomplished by this technique. (b) Optical image of a sample prepared for measurements. The dashed lines suggest areas most suitable for the respective measurement technique based on the density of nanostructures.

Measurement techniques like scanning photoelectron microscopy and photoelectron emission microscopy require the deposition of singled out nanostructures. Here, the tissue method demonstrated in figure 2.7a is more suitable. A triangular shape is cut out of cleanroom paper and swiped over the growth and subsequently the measurement sample. This allows for the deposition of only a few scattered nanosheets. In order to find distinct features for each measurement, pre-patterning of the sample via metal deposition and electron-beam lithography is advisable combined with surface mapping via scanning electron microscopy (SEM) as demonstrated in figure 2.7b. This method enables the consecutive investigation of the same nanostructures after respective process steps.

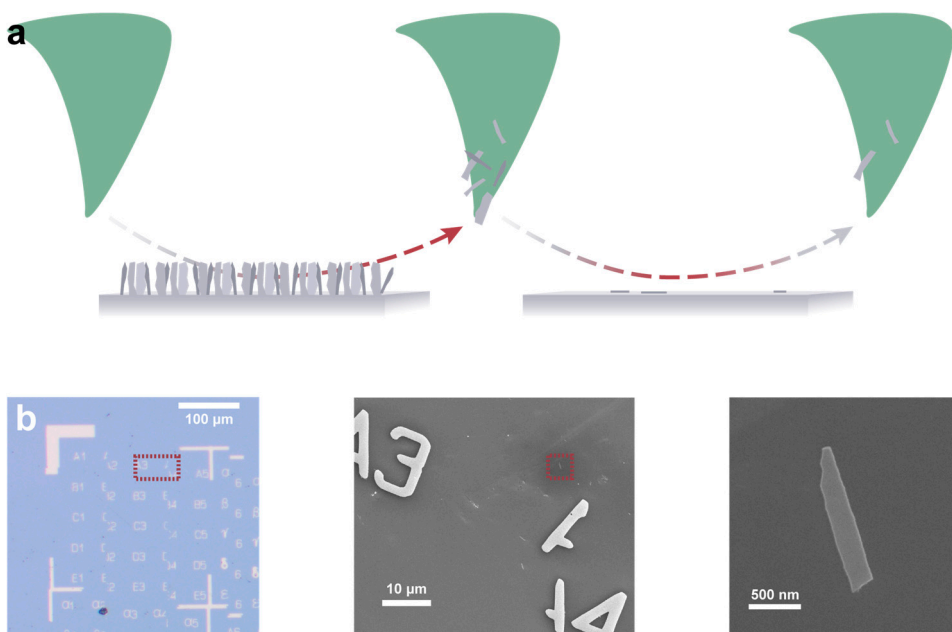


Figure 2.7 (a) Schematic of the tissue technique for depositing nanostructures with a low density. (b) Sequential zoom-in of optical microscopy and SEM images demonstrating the advantage of prior deposited metal markers on the substrate.

3 Characterization Methods

As we have met our heroines for the upcoming adventures, it is important to consider the means of storytelling. Each one of them highlights a different aspect. In the following, we will encounter ways on how to expose the outer and inner values of our main characters without immediate destruction. This part will set the scene for all upcoming endeavors by introducing the techniques employed in the presented studies to investigate the structural, chemical, and electronical properties of III-V surfaces.

Note, this chapter does not aspire to explain each method in detail. Rather, it will provide the base knowledge of the employed measurement techniques to understand the results shown and follow the discussion. For interested readers, literature recommendations for more in-depth information will be provided.

3.1 Scanning Tunneling Microscopy

Scanning tunneling microscopy (STM) is a direct imaging technique that can provide atomic resolution and information regarding the topography as well as the local density of states (LDOS) of the substrate surface. The basic setup requires a tip³ to raster scan over the surface of a conductive sample with a bias applied between both. This initiates electrons to travel from tip to sample or vice versa, which are recorded as a current signal.

Figure 3.1 displays the basic components of an STM. To approach the sample and raster scan over the surface, piezo motors are commonly employed. They enable precise positioning within sub-Ångström ranges. While the piezo in z-direction

³ In my case, the tips were made from tungsten and electrochemically etched with an NaOH solution (2 mol/l) followed by a subsequent sputter and annealing cycle in the UHV chamber. Other conductive materials (e.g. Au or Pt) are also possible as tips.

allows for distance control between tip and sample, the x- and y- motors facilitate movements over the surface. A feedback controller is also necessary. The feedback compares the pre-set current to the actual one measured and subsequently leads to position adjustments of the tip with respect to the sample. When the detected current exceeds the set value, the tip is retracted from the surface and vice versa for a current that is too small. Typical values for approaching and scanning are in the low to mid-pico Ampere range for III-V surfaces. Noteworthy, the apex of the probe and the sample surface are not in direct contact when approached. Thus, electrons need to tunnel (hence the name) through a gap of less than 2 nm when a bias is applied.

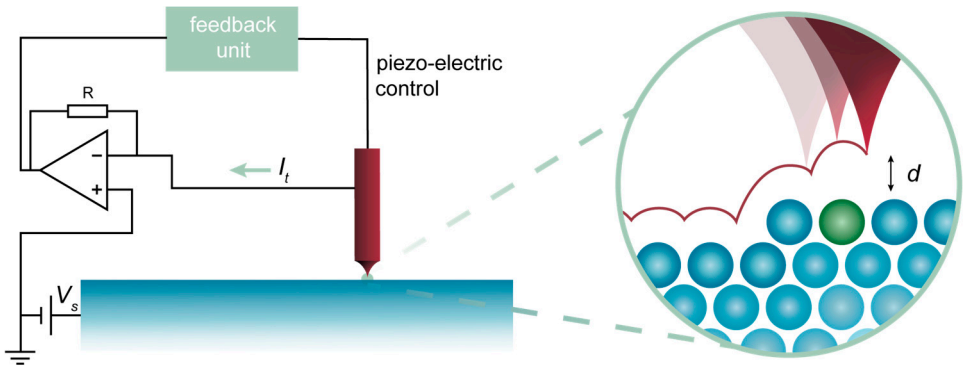


Figure 3.1 Schematic of an STM setup displaying the scanning tip, measured tip current I_t , the bias V_s applied to the sample, the feedback unit used for constant current scanning and the piezo-electric control. The red line in the zoom-in shows the projected tip movement over a sample exhibiting step edges and areas with different LDOS.

Short dive into the theory

To understand the origin of the signal measured in STM, Tersoff and Hamann⁶⁹ developed an approximation for the tunneling current based on the time-dependent Schrödinger equation and Bardeen's formalism⁷⁰. In their approach, they combined the limits of low temperature (no charge carriers are available above the Fermi level (E_F)), small voltages (a bias of meV is needed to scan on metals) and a point-like tip. As a result, the tunneling current I can be expressed as

$$I \propto V * \rho_s(E_F) * \rho_t(E_F) * e^{-\frac{2d}{\hbar} * \sqrt{2m\Phi}} \quad (3.1)$$

with V being the voltage applied between tip and sample, $\rho_s(E_F)$ the density of states (DOS) of the sample and $\rho_t(E_F)$ the DOS of the tip at the Fermi energy E_F , respectively, as well as d the sample-tip distance, m the electron mass and Φ the height of the potential barrier (averaged work function of tip and sample). ρ_t is a constant as the apex of the tip is approximated by an s-orbital. Unfortunately, scanning on semiconductors requires a bias about 10-100 times larger than on metal. Therefore, the linear approximation needs to be modified to

$$I \propto \rho_t \int_0^{eV} \rho_{s,loc}(z, E_F + \epsilon) d\epsilon. \quad (3.2)$$

We now consider the local density of states (LDOS) $\rho_{s,loc}$ at the tip position d integrated over an energy range defined by the applied bias (the origin of the electrons is also depicted in figure 3.2). Therefore, the tunneling current is dependent on three parameters: (i) the bias applied, (ii) the LDOS of the sample, and (iii) the distance between the tip and the sample. As a result of the dependency between I and d , the tunneling current decreases by a factor of 10 when the distance increases by about 1-2 Å. As a result, even a blunt tip can provide atomic resolution as long as one atom is positioned a bit closer to the sample compared to the rest.

Employed scanning mode

Due to the described relationship, two scanning procedures are possible with STM: constant current and constant height mode. All images in this book have been taken in constant current mode, i.e. the internal feedback adapts the tip-sample distance in order to keep a certain set value for the current. This way, the changes of the tip in z-direction are imaging the topography and LDOS of the sample. To detangle this information, images with the same field of view but different biases can be recorded as done in **paper II**. In general, larger biases are less sensitive towards the LDOS

and the signal is dominated by topographic information, as depicted in figure 3.2, and vice versa applies for lower voltages.

Imaging compounds

As InAs and GaAs are compound semiconductors, it is possible to distinguish between elements of group III and V by adjusting the scanning voltage. For both materials, As atoms receive electrons from In (or Ga) and contribute mostly to electronic states in the VB (= filled states). Empty states in the CB correspond mainly to unoccupied energy levels from In and Ga. Therefore, negative sample bias will image As atoms and positive bias group III elements. The electron movement between tip and sample for different applied biases are shown with blue arrows in figure 3.2.

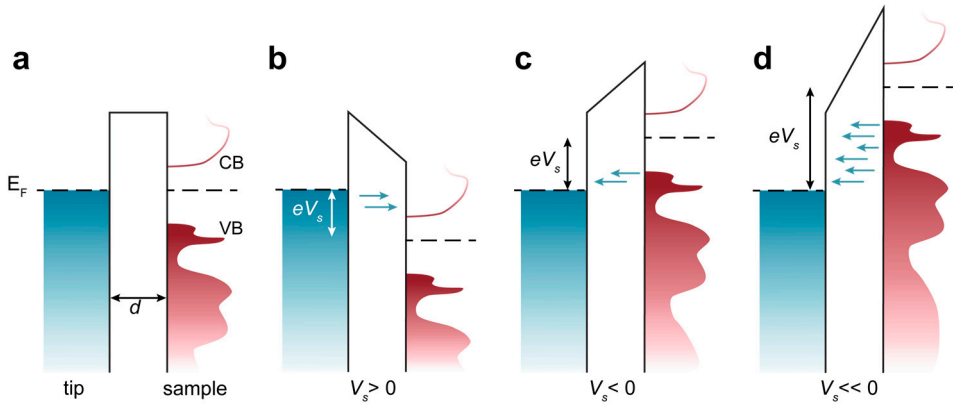


Figure 3.2 Schematic of the band alignment between tip and sample after the final approach without bias (a), with positive sample bias (b), as well as with small (c) and large (d) negative sample bias. For smaller voltages applied, the LDOS of the sample influences the signal significantly. For larger biases, this effect averages out due to the larger number of available electrons for tunneling. The tunnel direction across the gap is indicated with blue arrows in (b)-(d).

Obstructions

In principle, STM measurements do not require vacuum. However, to avoid surface contamination via oxidation or adsorption of molecules present in the atmosphere, a base pressure of min 10^{-9} mbar in the analysis chamber is advisable for high resolution images corresponding to ultra-high vacuum (UHV). Additionally, high voltage is needed for the piezo elements which can become problematic in atmospheric pressure.

Furthermore, the system should be decoupled from mechanical and electrical noise to achieve atomic resolution. Any outside perturbation easily overshadows the signal of the atomic rows from the sample surface. In our labs, this is facilitated via vibrational isolation of the whole setup from the surrounding building with additional suspension of the STM within the chamber by springs and magnetic damping.

As described in the theory section above, the tip is imagined as constant and isotropic with a single atom at the apex. This approximation gets disenchanted quite quickly when faced with reality. Variations of the orbital and/or number of atoms at the tip apex can promote different observations of the same sample area⁷¹. The effect of a multiple tip on InAs(11 $\bar{2}$ 0) nanosheets with incorporated Bi atoms as an example is shown in figure 3.3. It is obvious that interpretation of the data needs to be done carefully. Therefore, an ideal tip with one atom at the apex is desirable. Several procedures can be tried to improve and stabilize the tip like dipping it into a metal surface or scanning with large negative bias^{71,72}.

More in-depth information on STMs can be found in the references^{73–75}.

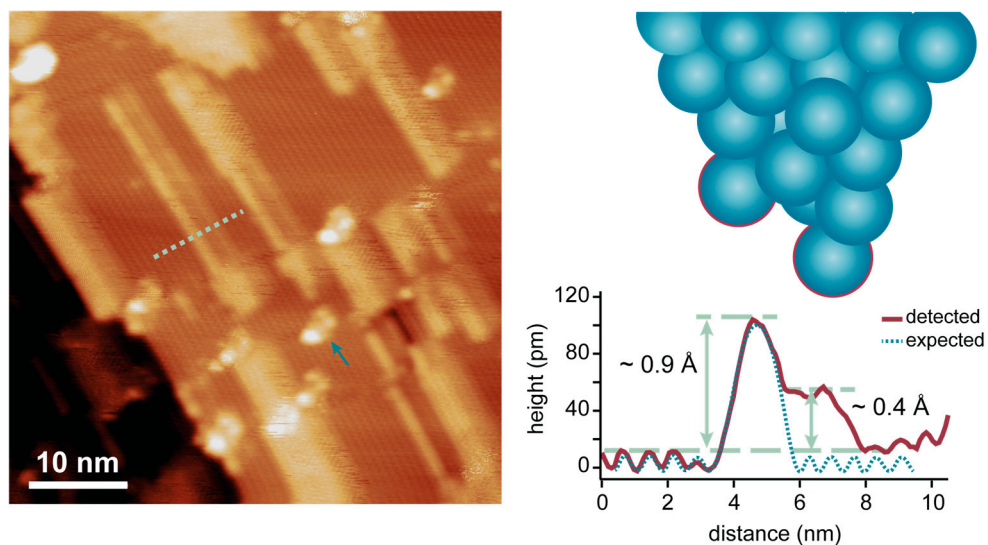


Figure 3.3 STM image on InAs(11̄20) nanosheets after Bi incorporation. The presence of a cluster with the same appearance all over the image (see blue arrow), as well as the shadow effect along the bright lines suggest the effect of multiple atoms participating in the scanning. As atomic resolution on the substrate is accomplished, one atom is closest to the surface. A possible atomic arrangement of the tip in one direction can be deduced from the line scan and is indicated on the right side. The solid, red line displays the recorded signal due to the tip and the dashed, blue line the expected surface morphology. Both atoms presumably participating in the electron tunneling are marked with a red outline.

3.2 X-ray Photoemission Spectroscopy

Chemical information of the sample can be accessed via X-ray photoemission spectroscopy. XPS is based on the photoelectric effect discovered by Albert Einstein⁷⁶, where electromagnetic radiation with a certain energy can excite electrons in a material to overcome the inner work function and be emitted. The work function is defined as the energy difference between the Fermi and the vacuum level for a material. However, E_F is usually positioned inside the band gap for semiconductors being hardly accessible. Therefore, the electron affinity (χ), difference between the vacuum level and the minimum of the CB, is more useful in this context. Dependent on the photon energy of the incident X-rays, electrons from the VB or deeper core levels can be excited. The photoelectron process and a corresponding XP spectrum are sketched in figure 3.4.

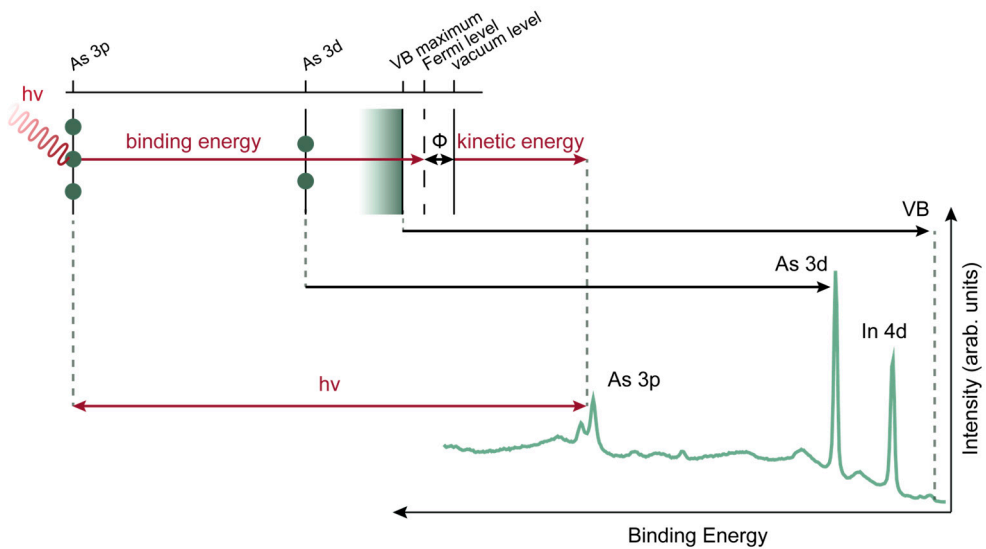


Figure 3.4 Illustration of the correlation between detected XPS signal (bottom right) and the energy conservation rule for photoexcited electrons from an As atom (top left). The spectrum is taken from an InAs sample, hence the In 4d core level peak.

Based on energy conservation, a direct relation between the kinetic energy of the photoelectron (E_{kin}), its binding energy (E_B), the work function of the material (Φ) and the photon energy of the X-rays ($h\nu$) can be derived

$$h\nu = E_K + E_B + \Phi \quad (3.3)$$

As mentioned above, determining the exact work function for a semiconductor material might be challenging. However, since analyzer and sample are in electrical contact, the kinetic energy of the electron measured in the experiment is relative to the work function of the analyzer (Φ_A)

$$E_B = h\nu - (E_K + \Phi_A) \quad (3.4)$$

Since core level electrons do not participate directly in bond formation with neighboring atoms they can serve as fingerprint for the respective element. As shown in section 2.2, as well as in **paper II** and **III**, the binding energy can shift dependent on the surrounding of the atom, e.g., surface atom compared to bulk, or bond formation with a different element. Therefore, XPS enables us to understand the composition of our substrate.

Measurement setup

The experiments presented in **paper I-V** were carried out at various synchrotron facilities within Europe (ASTRID in Denmark ⁷⁷, Elettra in Italy ⁷⁸, and Max IV in Sweden ⁷⁹). In contrast to a lab source, synchrotrons allow for, among other things, a wide range of available photon energies, a higher brilliance⁴ and smaller beam spots ⁸⁰. Especially the tunability of the photon energy enables depth-profile measurements, increasing the signal intensity for different orbitals governed by their individual photoionization cross-section, as well as easy comparison between core level signals of different elements by keeping the kinetic energy constant. Essential for high resolution spectroscopy is not only the source but also the analyzer used. Figure 3.5 shows an enlarged view of the electron trajectory in a hemispherical electron analyzer (EA) after being emitted from the surface. Electrons are counted based on their kinetic energy and emission angle. Before entering the analyzer, the

⁴ Brilliance is defined as the flux per unit area of the radiation source per unit solid angle of the radiation cone per unit spectral bandwidth.

incoming electrons are decelerated by electrostatic lenses to energies within the range of a so-called pass energy. This energy determines which electrons can pass the hemispherical analyzer to the detector. A potential applied between both curved plates serves as filter. In general, a larger pass energy enables more electrons in a wider range of E_{kin} to reach the detector. This results in a high signal intensity but limits the achievable resolution at the same time. Commonly, multi-channel plates or delay line detectors are used to collect the XPS signal at the exit slit.

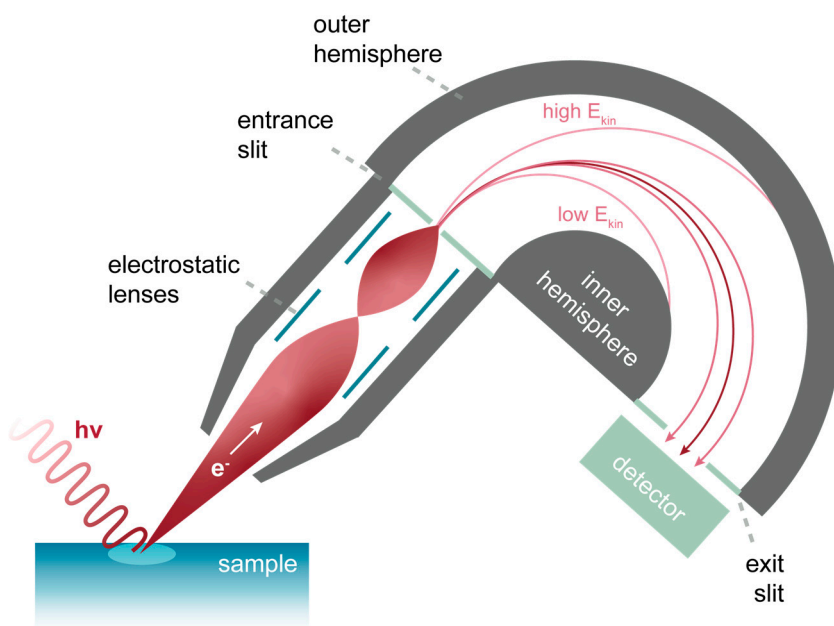


Figure 3.5 Sketch of the analysis setup for XPS measurements. The emitted electrons are magnified and focused before entering the hemispherical analyzer. Due to the potential applied between the outer and inner hemisphere the electron trajectory through the EA depends on their individual E_{kin} .

In general, XPS measurements require UHV conditions due to the large distances between sample surface and analyzer entrance slit⁵. As a rule of thumb, the electron

⁵ Ambient pressure XPS measurement balance the increase in pressure by a very small distance between sample and analyzer, as well as differential pumping.

mean free path in 1 mbar pressure is about 1 mm. Therefore, pressures preferably in the 10^{-11} - 10^{-9} mbar regions are required especially for extended data acquisition.

Soft X-rays

For the experiments presented, photon energies in the range from 100-700 eV were mainly employed corresponding to the soft X-ray regime. This allows for very surface sensitive measurements based on the inelastic mean free path of excited electrons as depicted in figure 3.6. In general, the excitation of electrons by X-rays with a normal incident angle can occur several micrometer deep in the substrate. The probability of electrons escaping the surface without inelastic scattering is mainly defined by electron-electron and electron-phonon interaction. Therefore, by choosing a photon energy corresponding to kinetic energies of around 70-100 eV, the probing depth can be as little as 2-5 Å corresponding to 1-2 atomic layers⁸¹. Figure 3.6 also indicates that by tuning the kinetic energy and ergo the photon energy, depth profiling is possible.

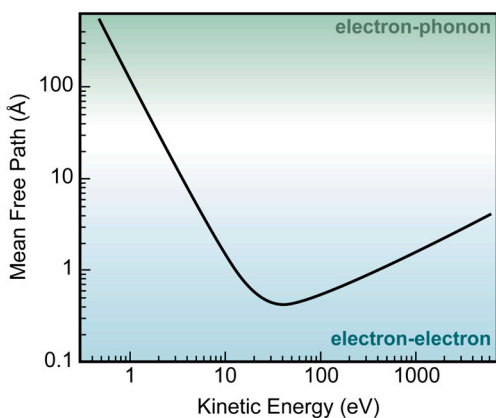


Figure 3.6 Inelastic mean free path of electrons dependent on their kinetic energy. This graph is also called the universal curve. Predominant scattering events are indicated in green and blue.

Analysis of the spectra

XPS peaks do not only display signals from the core level and VB electrons. As can be seen in figure 3.7, a decaying background with decreasing binding energy is also

detected. Excited photoelectrons can experience multiple inelastic scatter events before escaping the surface leading to a broad, staircase like background. I removed the background with a Shirley function⁸² in all spectra presented in this book. Fitting the actual core level peak was done by using a pseudo-Voigt function⁸³. The function approximates the convolution of a Gaussian (representing the signal broadening induced by the setup) and a Lorentzian (representing the broadening of the core-hole lifetime⁶).

Interestingly, all orbitals, with a core level number $n > 0$, exhibit core level peaks at two different binding energies (so-called doublet) with a fixed distance between them (so-called spin-orbit splitting). This is a result of the interplay between electron spin ($s = \pm 1/2$) and angular momentum (l), and characteristic for each element and orbital. As the total angular momentum is given by $j = |l \pm s|$, the notation for the Bi 4f core level peaks follows as Bi 4f 5/2 and Bi 4f 7/2 for the signal at higher and lower binding energy, respectively.

When several components are present in a single peak, the variety of fitting parameters can be reduced with careful consideration:

- the width of the Lorentzian must be constant for all components inside the same core level
- each component must be present in both parts of the core level doublet with a constant spin-orbit splitting
- the intensity ratio between the two parts of a doublet follows roughly $1/2$ for a p-, $2/3$ for a d- and $3/4$ for an f-orbital
- a bond between two different elements should be detectable in both elemental core level spectra

⁶ Based on Heisenberg's uncertainty relation, the lifetime of a core-hole decreases for states closer to the nuclei due to an increased number of available electrons in higher energy levels to fill it.

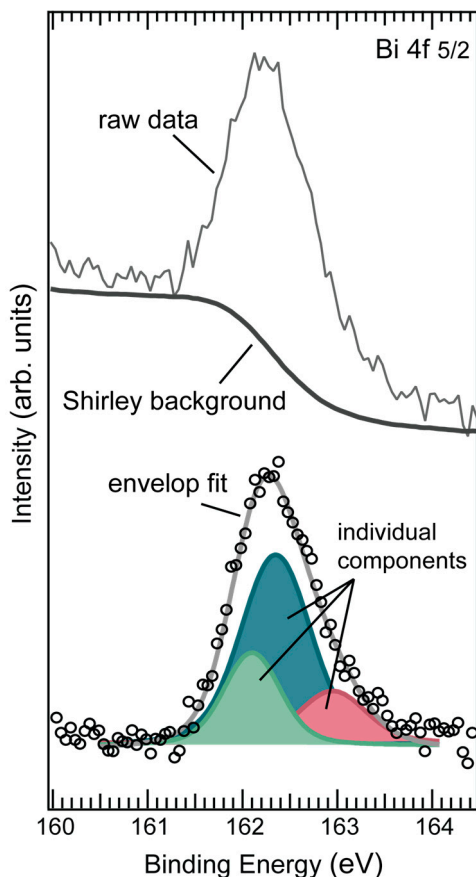


Figure 3.7 Evolution of XPS data analysis carried out in this work. After accounting for the Fermi level shift, the background was removed with a Shirley function. The number of implemented components is governed by the overall fit of the envelop function, reasonable values for the Lorentzian and Gaussian widths based on literature and if the same component can be detected for the second corresponding element involved in bond formation. Black circles are the recorded measurement points.

To move from qualitative to quantitative analysis, several additional effects need to be considered. A calibration of the exact Fermi level position is required. Here, a reference sample, like Ta or Au foil, is measured with the same photon energy as the sample. By comparing the measured binding energy with values from the literature the induced shift from the beamline setup can be accounted for. Furthermore, it is important to realize that the photoionization cross-section of individual core level varies for the same photon energy, as depicted in figure 3.8 for As 3d and In 4d core level peaks. Most of the spectra taken in my work concern photon energies around 100-120 eV for surface sensitive measurements (pink colored region). It is evident that the intensity of the As 3d peak will naturally be larger compared to the In 4d signal for pristine InAs substrates, also observable in

figure 3.4. Aside from misinterpretation of chemical compositions, this can lead additionally to a different number of sweeps taken for each spectrum⁷. Therefore, especially when the composition of a compound or the amount of material deposited needs to be extracted, these influences need to be considered.

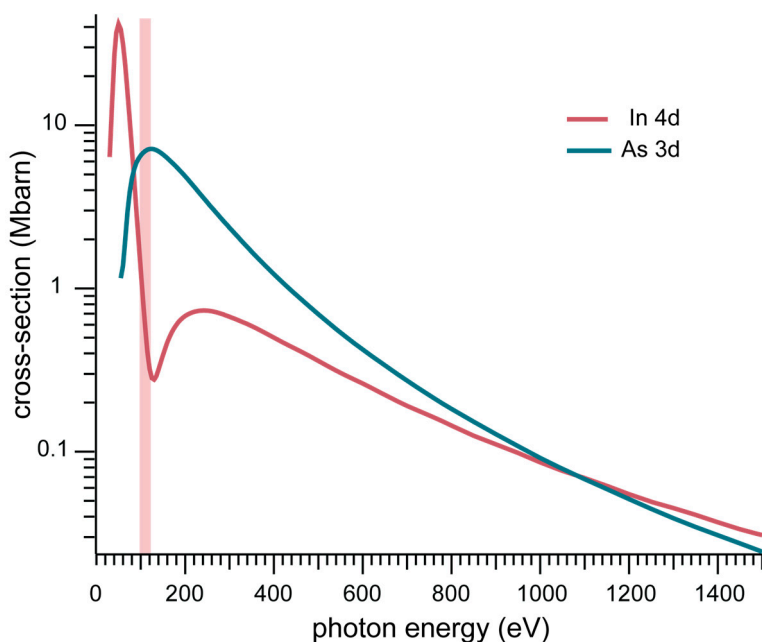


Figure 3.8 Comparison of the photoionization cross-section for the As 3d and In 4d core level with respect to varying photon energy. Data was taken from the Elettra website ⁸⁴.

⁷ Usually, the number of sweeps is adapted for each core level spectrum scan to guaranty a good signal-to-noise ratio. Higher intensities of the core level peak will automatically reduce the number of sweeps.

3.3 X-ray Photoemission Electron Microscopy

X-ray photoemission electron microscopy (XPEEM) is a direct imaging technique based on photoemitted electrons excited via X-rays. Here, the whole field of view contributes to the signal and information on the structural, chemical, electronic, as well as magnetic characteristics of a sample can be obtained. The electrons leaving the surface are accelerated to several keV, magnified, and refocused via electrostatic lenses before entering a hemispherical electron analyzer and hitting a 2D detector. For all XPEEM measurements, I used the aberration-corrected spectroscopic photoelectron and low energy electron microscope (SPELEEM) at the MaxPEEM beamline (Max IV, Sweden)⁸⁵. A representation of the setup is depicted in figure 3.9.

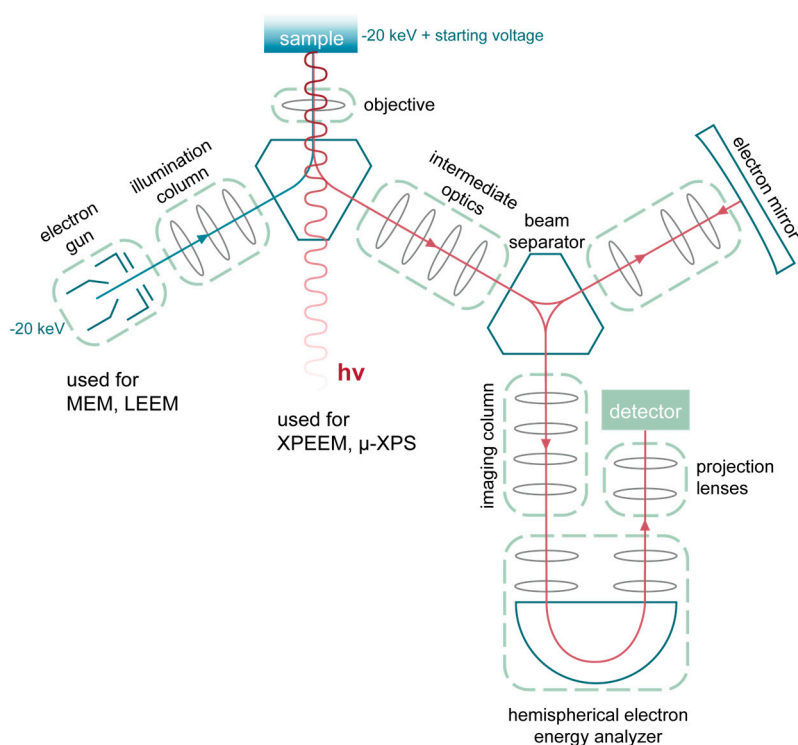


Figure 3.9 Schematic setup of the SPELEEM system at MaxPEEM at the Max IV synchrotron. Three modes of excitation are available: electron gun, X-rays and a UV-lamp (not depicted). The electron trajectory is marked in blue (to the sample) and red (to the detector). Electrostatic lenses are simplified by grey ellipses. The aberration correction is achieved via the electron mirror.

Two types of electrons can be detected: (i) secondary electrons, and (ii) core level electrons. Secondary electrons originate from states close to the Fermi level and allow to investigate differences in the work function of specific regions⁸. More relevant for my work were measurements involving core level electrons as implemented in **paper I** and **III**. By sweeping the photon energy, core level data comparable to XPS signals can be acquired (see figure 3.10 as an example). Here, the energy and spatial resolution can be below 0.2 eV and 20 nm, respectively⁹.

As for XPS, UHV conditions are required and the escape depth for the detected electrons follows the dependency described above. However, due to the large negative bias applied to the sample accelerating the electrons into the beam separator, all electrons ejected from the surface arrive at the analyzer in contrast to XPS.

Interestingly, μ -XPS measurements are also possible with the SPELEEM setup increasing the energy resolution to below 0.15 eV. Here, the dispersive plane of the analyzer is imaged by inserting apertures into the electron path. Furthermore, the aperture in the image plane limits the area photoelectrons are collected from the sample allowing for very local probing of the surface chemistry.

Further detailed information on the overall setup, aberration correction, electron-sample interaction and more can be found in ^{86,87}. The advanced SPELEEM setup at MaxPEEM allows for a combination of additional techniques with XPEEM. The most relevant ones for my work will be explained shortly below.

⁸ These can originate from different compositions or crystal facets ¹⁴⁷.

⁹ During the summer of 2023, the analyzer has been updated allowing for better energy and spatial resolution, as well as a higher acquisition rate for recording movies.

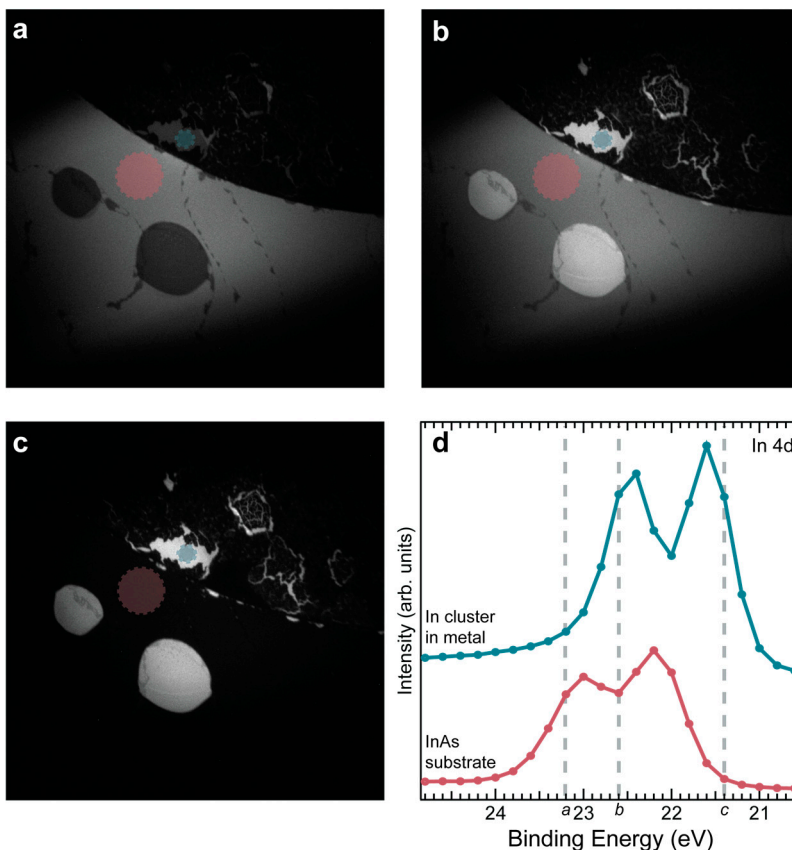


Figure 3.10 (a-c) XPEEM images for different photon energies in order to investigate the presence of In in the area of interest after annealing the sample. The lower part of the image consists of an InAs(111)B substrate with In droplets (round, bright areas in (b) and (c)) and the upper part consists of an Al/Pd metal stack into which In atoms diffuse during annealing. The field of view is $50 \times 50 \mu\text{m}^2$, respectively. Contrast settings were the same in all images to signify the signal intensity of each region. (d) In 4d core level spectra taken from the XPEEM sequence (step size 0.2 eV) in the regions indicated by the shaded areas in (a-c). It is evident that areas with different chemical composition can be easily detected via XPEEM and further curve fitting of individual components is possible.

Signals from elastically backscattered electrons

As shown in figure 3.9, the SPELEEM system includes an electron gun, illumination column and beam separator in front of the objective lens not necessary for XPEEM measurements. These components allow for full-field imaging of the

surface via backscattered electrons. This facilitates real-time data acquisition and therefore *in-situ* studies as carried out in **paper I**. In general, electrons emitted via an electron gun are focused on to the surface. The sample exhibits a bias of -20 kV decelerating the incoming electrons. This allows for surface sensitive interaction due to the low energy of the electrons. This interaction is governed by the potential difference between gun and sample (also called starting voltage). After reversing their trajectory, the electrons are once more accelerated and follow the same path as photoelectrons in XPEEM. In order to split the incoming and outgoing electron signal, the beam separator is redirecting each signal with a 60° angle. There are two measurement techniques possible depending on the starting voltage.

Mirror electron microscope

Here, a low starting voltage inhibits that electrons reach the sample surface, and their trajectory is reversed tens of nanometer above¹⁰. As a result, the incoming charge carriers only interact with the electric field of the substrate. Contrasts arise due to changes of this electric field based on varying surface composition or changes of the electric and magnetic field of the sample among others^{88,89}. This mode is called mirror electron mode (MEM). Images are not easy to interpret, since well-defined features, mapped before by SEM, can appear very differently in size and shape.

Low energy electron microscope

By moving towards higher starting voltages (equal to higher kinetic energies), electrons directly interact with the sample surface via scattering. Generally, the detected contrast in the image originates either from local differences in the crystallographic arrangement of the surface atoms (diffraction contrast), or interference of the reflected electrons from different depths due to surface steps or buried interphases (phase contrast). This mode is called low energy electron mode (LEEM). By removing the contrast aperture in the focal plane, a diffraction pattern

¹⁰ This is especially suited for samples suffering from electron induced damages, e.g. biological samples.

can be detected resulting in a low energy electron diffraction (LEED) signal for ordered surfaces.

In my work, both MEM and LEEM were mainly used for overview images of the surface and to identify specific measurement positions. Deeper analysis was then carried out via XPEEM and μ -XPS measurements. More information on both elastic backscatter techniques and the interaction of electrons with the substrate surface can be found in the thesis by Martin Hjort ⁷¹.

3.4 Angle-resolved Photoemission Spectroscopy

Angle-resolved photoemission spectroscopy is an advancement of XPS and enables the direct mapping of the electronic band structure in crystalline materials for occupied states. In general, the emitted photoelectrons are analyzed based on their momentum additionally to their energy. Similar to energy conversion, momentum conversion also applies for electrons leaving the surface. However, due to the refraction at the surface-vacuum interface and the loss of periodicity along the surface normal, only the in-plane momentum ($k_{||}$) of the photoemitted electrons is preserved. It is dependent on the polar emission angle (ϑ) ⁹⁰, and can be calculated based on:

$$k_{||} = \frac{1}{\hbar} \sqrt{2mE_{kin}} * \sin \vartheta \quad (3.5)$$

with \hbar being Planck's constant, m the electron mass and E_{kin} the kinetic energy. A more detailed approach can be found in ⁹⁰. Based on equation 3.5, the in-plane dispersion $E_B(k_{||})$ can be measured by varying ϑ .

An example of an ARPES spectrum of an InAs(111)B surface after oxide removal is depicted in figure 3.11. Several parabolic bands symmetrical around the Γ -point with varying dispersion are visible. It is evident that the Fermi level is positioned inside the band gap, therefore only the energy states in the VB are visible. For more complex material systems, comparison to band structure calculations (as shown in

figure 2.4) is very useful to understand the origin of the respective energy bands ⁹¹ and the contribution of individual elements, as shown in **paper II** and **V**.

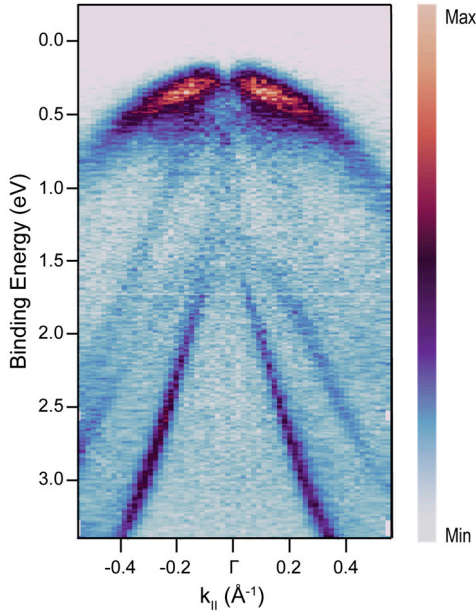


Figure 3.11 ARPES spectrum of a pristine InAs(111)B surface in normal emission with the Fermi level positioned inside the band gap. The Γ -point corresponds to $k_{||} = 0$. The spectrum is taken along the M- Γ -M direction in the Brillouin zone.

Considering an ARPES setup, the analyzer accepts electrons only from a small finite angle. As a result, the photoelectron density can be linked to E_{kin} , the polar angle (θ) and the azimuthal angle (φ) of the electron trajectory. To map out the whole band structure of the Brillouin zone, rotation of the sample is necessary. A schematic setup and the influence of changing angles between the sample and electron trajectory are displayed in figure 3.12a. How the in-plane dispersion can be mapped out within the first Brillouin zone and beyond by adjusting the sample position with respect to the analyzer is indicated in figure 3.12b. Alternatively, the electron analyzer can be moved to map out the band structure¹¹.

¹¹ This is usually more intricate since the whole setup is in UHV conditions. However, moving the analyzer allows for a high stability regarding the measurement position on the sample surface especially interesting for μm - or nm -sized specimen.

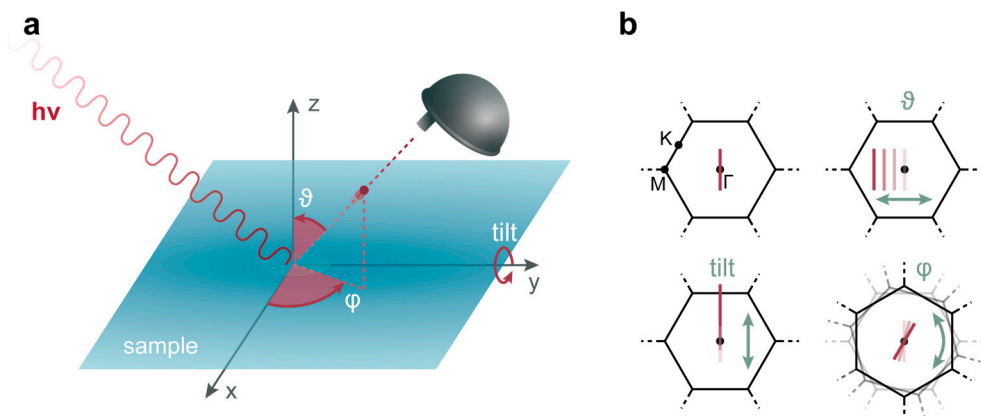


Figure 3.12 (a) Geometry of an ARPES experiment. The electron is represented as red circle and its emission trajectory is defined by the polar (θ) and azimuthal (ϕ) angle. (b) Effect of changes in θ , ϕ and tilt of the sample on the measurement area within the Brillouin zone (top view). The sample exhibits a hexagonal symmetry and important symmetry points are marked exemplary in one position. The indicated measurement area (red line) scales with the acceptance angle of the analyzer and kinetic energy of the electrons. Here, the analyzer slit is vertical. The dependencies for the tilt and θ switches for a horizontal slit arrangement.

Compared to XPS, the employed photon energies are typically low as a result of the photoionization cross-section of VB electrons. However, the achievable energy and momentum resolution is higher⁹². Due to the very small inelastic mean free path of electrons at photon energies in the range of 10-120 eV, ARPES is extremely surface sensitive. As a drawback, depth profiling is very limited and anisotropy along the surface normal will not be accessible¹². However, electrons exhibiting kinetic energies and emission angles within a certain range can be detected simultaneously with the employed 2D detectors. In general, ARPES enables the analysis of electronic, chemical, and magnetic¹³ properties⁹³.

Similar to XPS, potential shifts of the Fermi level induced by the setup can be accounted for by considering the work function of the analyzer and equation 3.4.

¹² Recent advances for ARPES setups have led to the implementation of hard X-rays (HARPES). Here, electrons several nanometers deep in the material will be detected. However, the signal of electrons with direct transition (ergo momentum conservation) decreases drastically.

¹³ Here, the detection of the respective electron spin is necessary.

However, this shift can be hard to determine for semiconductors when E_F is positioned inside the band gap. As the work function of the analyzer is the defining parameter, all samples will exhibit E_F at the same position. Therefore, determining the Fermi level shift on an arbitrary metal sample will allow once more for an energy correction.

Accessing the perpendicular momentum

As mentioned above, the momentum normal to the sample surface (k_\perp) is not preserved for the emitted electrons. However, by assuming a free-electron like final state, values for k_\perp can be approximated via

$$k_\perp = \frac{1}{\hbar} \sqrt{2mE_{kin} \cos^2 \vartheta + V_o} \quad (3.6)$$

$V_o = |E_o| + \Phi$ corresponds to the bottom of the VB with respect to the vacuum level and is called the inner potential⁹⁰. Olsson et al. determined the inner potential for InAs(111)B to be 8 eV after observing signal maxima at 20 and 44 eV⁶³. Experimentally, k_\perp can be accessed more easily by measuring the photoelectrons in normal emission. Here, the detected signal for varying photon energies corresponds to the dispersion along k_\perp .

Furthermore, equation 3.6 enables us to roughly determine at which photon energies symmetry points in the Brillouin zone will be detectable, as shown in **paper IV** for the InAs WZ (11 $\bar{2}$ 0) lattice. Here, k_\perp values are determined by the lattice vector along a specific crystal direction in reciprocal space. A further multiplication with $n = 1, 2, 3, \dots$ allows for an estimation of the distance between the Γ -points in the first and second ($n = 2$), or the third Brillouin zone ($n = 3$) etc. By combining equation 3.4 and 3.6 and assuming $E_B = 0$, the photon energies, at which a signal for the respective Γ -point is expected, can be calculated. As will be demonstrates later, this method also allows to determine photon energies for other symmetry points of the Brillouin zone.

4 Sample manipulation

An unknown journey lies ahead of our III-V heroines. We will dive right into their adventures leading us into the maze of chambers, caves and grottos. In this chapter, I will introduce different methods on how the native oxide of the compound materials was removed after being introduced into UHV. Starting from the clean surface, two main storylines will unfold: (i) changing the concentration of freely diffusing atoms on the InAs surface during high temperature annealing via metal patterns, and (ii) the manipulation of III-V surfaces via Bi deposition. Findings presented in **paper I-V** will not be discussed in detail, but rather the main conclusions highlighted.

There are two main villains in this book. One is time e.g., in the form of process duration or waiting time. Due to its nature, time usually strikes slowly, lurking on tiptoes on the corners of ramping procedures, transfer processes or equipment malfunction. On occasion, it utilizes temperature in order to maximize its force. I will address the influence of time on one of the protagonists further below.

The other villain is the pressure, to be more precise the atmospheric pressure or vacuums of low quality ($> 10^{-9}$ mbar). This antagonist strikes ravaging, without differentiation nor reservation. As all the investigated III-V semiconductor surfaces are exposed to the atmosphere at some point during their journey from synthesis to our sample holders, oxidation of the surface is a common problem. The next section will focus on how to remove this native oxide. It is noteworthy, that in order to avoid oxidation of specific surfaces, interlayers or interfaces capping layers can be evaporated onto the sample as in the case for **paper V**. This sacrificial layer is then removed in UHV to reveal the layer of interest without any contamination.

4.1 Removing the native oxide

To have any success and longer lasting effect of the native oxide removal, it is essential that the sample is brought into a UHV chamber (with a minimum base pressure of 10^{-9} mbar) for all of the procedures described in the following.

Metallic surfaces are commonly cleaned via several cycles of sputtering and annealing. Here, the surface is bombarded with accelerated Argon ions and subsequently annealed. This is disruptive process for the crystal structure since adatoms on top as well as the surface layer and lower sitting atoms are propelled out of the crystal lattice by the force of the impinging atom. The high temperature annealing step afterwards is essential to heal the lattice structure and surface. The technique of sputtering and annealing is also very common to remove the native oxide of semiconductors. However, several problems arise here for compound materials. One element might be sputtered more easily than the other^{94–96} leaving a surplus of the other on the surface. This can result in a high density of defects in the top layer. Subsequent annealing might enhance this problem. Consequently, reconstructions of the surface are often observed.

Hydrogen treatment

Removing the native oxide with atomic Hydrogen prevents the excessive formation of defects and can therefore inhibit a reconstruction of the surface. Here, the sample is brought to a target temperature (about 400°C for InAs and 500°C for GaAs) while being exposed to atomic Hydrogen, generated by a thermal cracker with an H₂ pressure of 2×10^{-6} mbar. For this molecular Hydrogen is thermally cracked in a so-called Hydrogen cracker by engaging with a tungsten wire heated to around 1700°C. Depending on the distance between sample and Hydrogen cracker, the annealing time can be as short as 20 min. An InAs(111)B surfaces after Hydrogen treatment is shown in figure 4.1. The atomic distance is 4.7 Å which is a bit bigger than expected but suggests that the surface is unreconstructed⁹⁷. The contrast adjustment enhances the perception of defects in the surface which are predominantly triangular shaped and aligned along the same direction. Earlier studies suggest that these are the result of In vacancies in the first layer⁹⁷. As a result, the adjacent As atoms have a different electronic contrast in the STM image and even relax towards the second

layer evoking the perception that all three As atoms are missing. The measured depth of ~ 1.6 Å corresponds well with the value in the literature and excludes the removal of all top layer atoms, since the height of an InAs monolayer is measured to be ~ 3.4 Å. However, single In vacancies do not account for the irregularly shaped defect indicated by the green arrow in figure 4.1a exhibiting a similar depth profile with ~ 1.8 Å. Due to the difference in vapor pressure, it is more likely for As atoms to leave the surface^{98,99} as is observed in **paper I** and discussed later. Therefore, missing As surface atoms cannot be excluded as the cause of the defect and additional measurements as well as DFT calculations are needed to gain a better understanding. Figure 4.1c shows a larger overview of the InAs(111)B surface with atomically flat terraces and step edges along the $\langle 110 \rangle$ directions typical for (111) surface¹⁰⁰. Here, the average height of the step edges is 3.6 Å corresponding to a monolayer (ML) of InAs⁹⁷ and in good agreement with figure 4.1b.

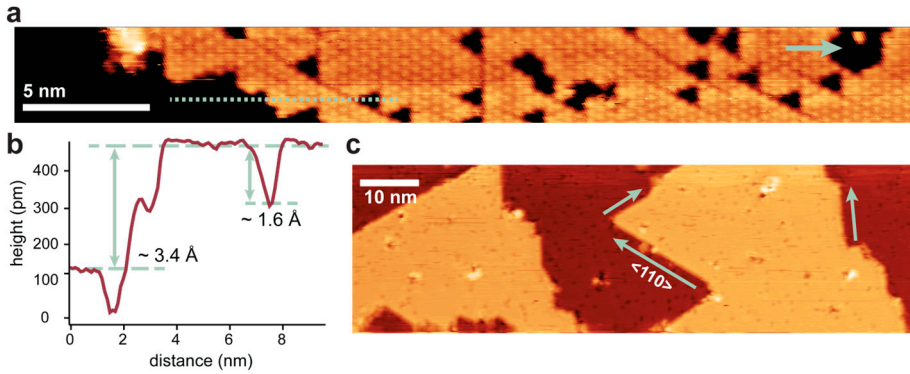


Figure 4.1 (a) STM image of an InAs(111)B surface after removing the native oxide showing triangular and randomly shaped defects in the top terrace. The contrast was adjusted to highlight the atomic resolution ($I=140$ pA, $V=-3$ V). (b) Lineprofile indicated in (a) for depth comparison of the defects and monolayer step size. (c) Larger overview STM image of a cleaned InAs(111)B surface. The arrows indicate the predominant step direction on (111) surfaces ($I=140$ pA, $V=-3$ V).

As mentioned in section 2.2, the nanosheets employed in **paper III** and **IV** exhibit a WZ $(11\bar{2}0)$ crystal structure intermitted by individual layers of ZB (110). This can be confirmed by determining the surface of a cleaned nanosheet by STM as shown in figure 4.2. I estimate that less than 10% of a single nanosheet is made of ZB (110)

layers by determining the atomic structure at several places on the surface for various nanosheets. It is important to notice that even though the synthesized specimens are of high crystal quality, there are vacancy defects present in the surface as can be seen in figure 4.2a. Furthermore, the overall appearance can vary among nanosheets of the same growth batch from a top facet fully covered by a single terrace towards several terraces being present and additional step edges exhibiting surface atoms (see figure 4.2b).

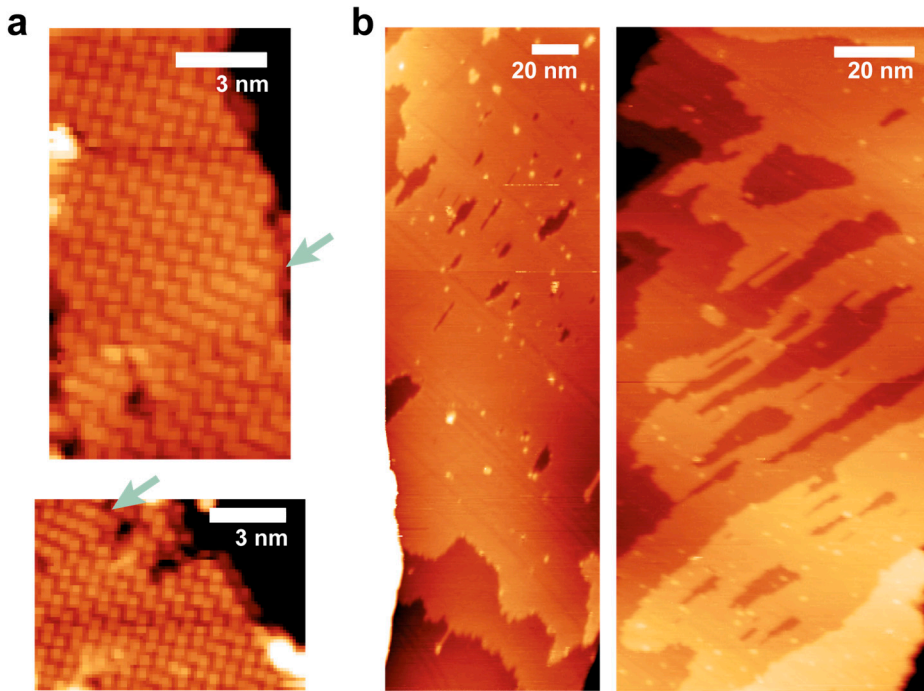


Figure 4.2 STM images of InAs nanosheets with WZ ($11\bar{2}0$) crystal structure after removing the native oxide. (a) The arrows indicate the small of ZB (110) layers present in the crystal structure. (b) Overview images of two different nanosheets displaying the possible variety of surface modification by vacancies and step edges. ($I=100$ pA, $V=-3$ V).

Oxide removal in an MBE system

When an MBE system is attached to the desired measurement techniques, the native oxide can also be removed by simply annealing the III-As compound semiconductor under As pressure. Furthermore, overgrowth of the substrate surface with a few nanometers of new III-V material can be added as shown in figure 4.3a for InAs(110). Here, the sample was heated to 460°C while being exposed to a simultaneous As and In flux for about 44 min with a layer growth rate of about 0.63 ML/s. Subsequently, the sample was annealed for 5 min at the growth temperature under As backpressure and cooled-down in UHV. The achieved surface quality was high and without reconstruction. A lattice distance of around 6 Å corresponding to a (1x1) surface was facilitated. The white protrusions observable in figure 4.3 are attributed to excess As atoms forming clusters.

Generally, As is more volatile compared to In or Ga and tends to go into gas phase already at lower temperatures. As a result, an As deficiency can occur on the surface introducing reconstruction^{53,101}. By supplying an As backpressure in the MBE chamber during annealing and cool-down, this can be counteracted. It is advisable to be cautious, however. A too high As pressure can also result in the deposition of additional As atoms and layers negating a high surface quality, as can be seen in figure 4.3b. Similar to a low As flux, surface reconstruction can also be introduced for a high As flux^{97,102}. However, we use a high As flux in **paper V** to deposit an As capping layer after exposing the InAs substrate to Bi. Here, it serves as a protection against oxidation of the InAs interface and more details will be given later.

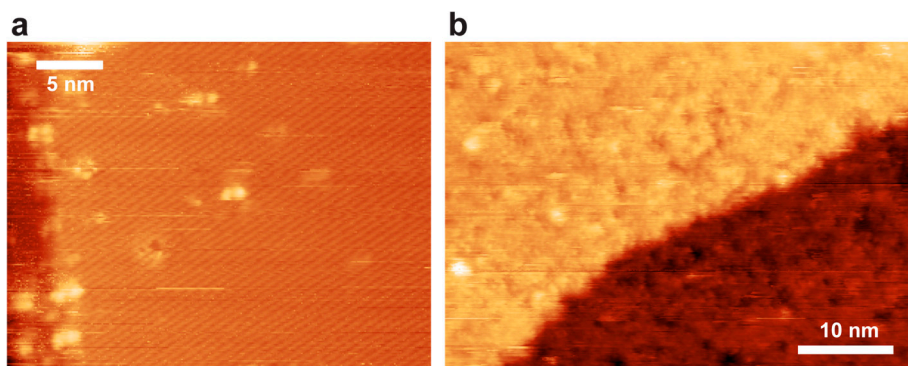


Figure 4.3 STM images of an InAs(110) surface after removing the native oxide and overgrow the surface with over 200 nm newly deposited InAs. (a) The As flux was shut-off during cool-down resulting in a high-quality, unreconstructed surface. (b) The As flux was left on during cool-down. The underlying surface structure is only vaguely visible due to the high coverage with excess As atoms. (left: $I=106$ pA, $V=-2.8$ V; right: $I=100$ pA, $V=-2.6$ V).

So right at the start of every adventure in this book, the quality of each III-V semiconductor specimen is tested on their ability to get rid of the native oxide. Seemingly an easy task performed by many before in various ways, some samples can be doomed as a result of equipment failure, geometric differences for individual UHV chambers or simply unlucky days. Their journey is cut short by ending in the trash pile. However, once cleaned the III-V heroines are well prepared for their upcoming endeavors, which I will describe in the following.

4.2 Droplet formation

After removing the native oxide of the III-V semiconductor a variety of opportunities to play, manipulate and interact with the surface come to mind. One of the simplest approaches is to raise the sample temperature. This will change the appearance of the surface eventually, since the InAs crystal will start to decompose. To be more precise, when heating above the congruent evaporation temperature T_c , As atoms will go into gas phase at a much higher rate compared to In atoms due to their difference in vapor pressure^{98,99}. As a result, an excess of In atoms will remain freely diffusing on the surface, subsequently forming In droplets on the micrometer scale. This effect is well known for III-V semiconductor compound surfaces^{27–29,103–105}. Interestingly, these droplets will not remain static once formed, but rather follow a distinct crystal direction while diffusing over the surface^{28,29,104}. As with many things in life, the phenomenon of droplet formation can be advantageous or unfavorable.

Droplets consisting of group III elements have been shown to enable the growth of a variety of nanostructures^{106,107}. Here, they act as seed particles for nanowires^{108,109} and quantum dots^{110–112} when interacting with a new precursor gas let into the reaction chamber. This way different III-V compounds can be combined on a single substrate via epitaxy^{108,113}. Furthermore, it was shown that the presence of droplets has significant influence on the synthesized crystal facets^{114,115} and the overall appearance of the nanostructure¹¹⁶.

On the other hand, the presence of μm -sized droplets on the surface is unfavorable for further device processing excluding nanostructure synthesis. The supersaturation of the surface with group III element atoms increases the surface roughness dramatically leading to an impaired interface quality. Furthermore, the implementation of ternary systems is limited since new precursors will predominantly interact with the single-element-droplet and not the III-V surface³⁹.

Droplet mitigation

Two approaches are most common to avoid droplet formation. One way is to set all process temperatures to be below the congruent evaporation temperature after the

implementation of the III-V layer. This restricts the temperature range of all following synthesis processes and consequently limits the range of potential applications. The other way allows for higher temperatures by heating the sample with a backpressure of the more volatile element. For InAs or GaAs, a backpressure of As is required. Automatically this demands the presence of a sophisticated chamber system, since As is highly toxic.

In **paper I**, we explore a different route to mitigate this low-dimensional phenomenon. By implementing lithographically metal stacks of Al (5 nm) and Pd (20 nm) on an InAs(111)B surface, the formation of μm -sized In droplets can be locally prohibited when ramping the sample temperature fast to a maximum of 600°C , as shown in figure 4.4a. This temperature is significantly higher compared to T_c found in literature for InAs(111)B^{28,117}. We investigated the surface with XPEEM and μ -XPS and found that the Pd layer acts as a sink for the In atoms freely diffusing on the adjacent semiconductor surface. Since the metal stack stays laterally confined, a diffusion of In atoms towards the pattern must take place. Furthermore, vertical diffusion of the metal stack into the InAs surface occurs. By tuning the thickness of the Al layer, the efficiency of the droplet suppression and the rate of vertical intermixing can be adjusted. The overall size and appearance of the droplet-free zone (DFZ) around the metal is governed by two factors: (i) the diffusion coefficient, and (ii) the solubility of In in Pd. Exposing the sample to temperatures above 650°C , the number of In atoms released from the surface exceeds the amount of available Pd necessary for effective alloying. Consequently, the DFZ vanishes, and droplets form everywhere (see figure 4.4b).

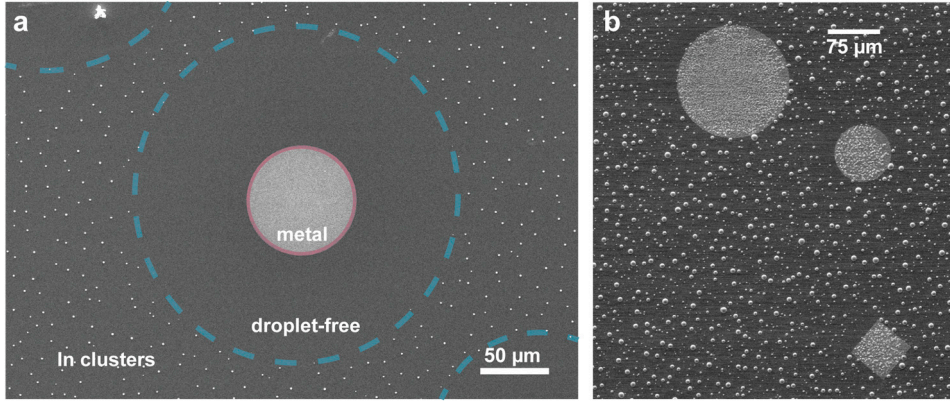


Figure 4.4 SEM images of the oxide-free InAs(111)B surface with Al/Pd (5 nm/20 nm) stack after annealing to 600°C (a) and 650°C (b) in a rapid manner. In (a), the emerging zones separated by the presence of micrometer-sized droplets are indicated. The images are reproduced from ¹¹⁸ (**paper I**) with permission from Springer Nature.

The DFZ can be maximized by implementing a smart pattern design and placement as discussed in **paper I**. Additionally, we show that the formation and size of the DFZ can be modelled based on a mass-balance and nucleation approach in good agreement with the experimental data. As this approach is based on the simple concept of In solubility in Pd ¹¹⁹, it should be possible to utilize it for a wide range of material combinations such as InP, InSb, GaN or GaAs with metals like Au ^{120,121}, Ti ^{119,122} or Pt ¹²³. All phase diagrams indicate various possible alloys between the substrate element and each metal for annealing temperatures above T_c of Ga- or In-V compounds. Further, the employed metal stacks can be used for electrical contacts reducing the number of necessary fabrication steps.

In-situ study

The above-described mechanism is robust in relation to different lithography processes, defects in and on the surface as well as pattern design (more details in **paper I**). However, if no attention is given to the process time, our III-V protagonist will be covered all-over in droplets similar to the case described in figure 4.4b. The effect of time is illustrated in figure 4.5 by presenting sequences from an *in-situ* study of an InAs surface with a sample temperature of 550°C taken in MEM mode

with the SPELEEM setup at the MaxPEEM beamline. This is well below the droplet formation limit of 650°C set by the rapid annealing study above. In the upper right side of each image, the edge of a metal stack consisting of 5 nm Al and 20 nm Pd is visible. The field of view is 50 μm x 50 μm . Therefore, we should not see any part of the droplet-zone visible in figure 4.4a. Nonetheless, a μm -sized droplet forms and starts to migrate after about 5 min. At the same time, additional droplets start to diffuse into the field of view indicating that the size of the DFZ is shrinking over time. The metal stack is approaching its limit of In solubility allowing for droplets to exist in the vicinity. This clearly demonstrates that a trade-off between process time and temperature needs to be considered when utilizing metal patterns to mitigate droplet formation.

Interestingly, distinct changes in the metal pattern are observable during the whole annealing process indicating the ongoing diffusion of In atoms into stack. As a result, nanometer sized droplets forming in the vicinity of the metal will start to decrease in size and subsequently vanish over time (compare the InAs surface of figure 4.5c and d).

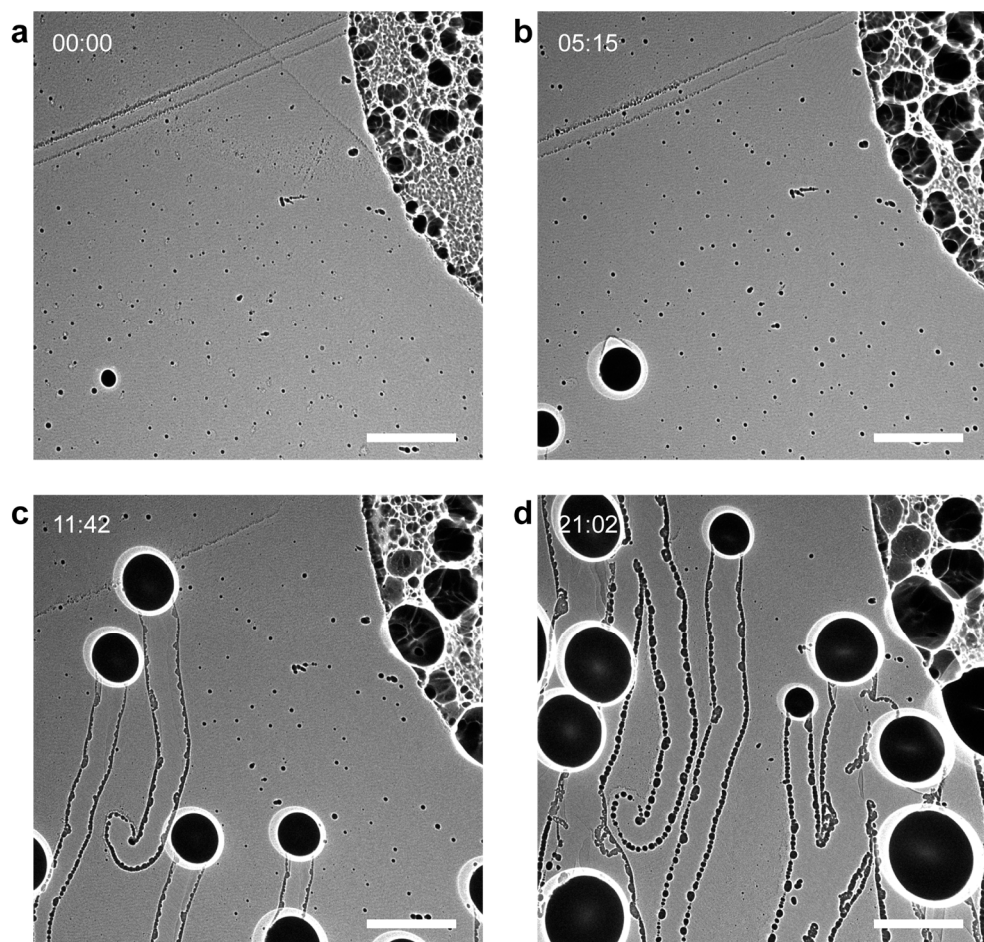


Figure 4.5 Images of an InAs(111)B surface taken in-situ with MEM at the edge of an Al/Pd (5 nm/20 nm) stack (upper right corner) after removing the native oxide. The sample temperature was kept at 550°C. Time stamps are indicated in the upper left corner. The scale bar is 10 μm , respectively. The images are reproduced from ¹¹⁸ (**paper I**) with permission from Springer Nature.

4.3 Manipulation via adatom deposition

The adventures described so far led our III-V protagonist into the world of UHV chambers where every breath taken means cutting your lifetime short. Here, their exterior was cleansed from any contamination brought with from the travels outside of the UHV. They experienced how wearing metallic ornaments with different compositions and shapes can enhance their resistance towards higher temperatures. Next, I want to show you how our heroines undertake the task of changing their skin and what might come of it.

There are several ways to introduce a new surface to a III-V semiconductor. Most commonly, synthesis via MBE with ¹²⁴ or without ^{125–127} the assistance of plasma, or metal organic vapor-phase epitaxy ^{128–131} (MOVPE) are employed. Magnetron sputtering ¹³² and atomic layer deposition ^{133,134} can also be utilized. The created heterostructures exhibit properties defined by the material combination and their interface. Among other characteristics, it was shown that III-V based heterostructures exhibit a 2D electron gases (2DEG) ^{135,136} at the interface, the bandwidth of usable wavelengths can be tuned for optoelectronic devices ¹²⁸, the breakdown voltage increases for nanowire transistors ¹³⁷.

The formation of III-Bi is very desirable due to the predicted enhancements in spin-orbit coupling ³³, localization of charger carriers and ergo increase in spin splitting ³⁶ as well as band gap engineering ¹³⁸, as mentioned before. However, the synthesis of III-Bi compounds via MBE processes has been proven to be challenging due to the low solubility of Bi in InAs or GaAs ¹³⁹. So far, a maximum integration of 22% for GaAs ⁴² and 6% for InAs ³⁷ is achievable without the formation of Bi clusters. In **paper II** and **III**, we present a new approach towards Bi integration into a III-As surface. Based on the study of Sb integration into the surface of GaAs ⁴³, we aim to create atomically sharp interfaces by depositing Bi atoms onto different III-V surfaces via a Knutsson cell evaporator and variations in sample temperature. This method allows for easy Bi integration due to the low amount of equipment involved (a UHV chamber, a heatable sample stage and a Knutsson cell evaporator).

In general, we explore two different synthesis routes demonstrated in figure 4.6 to enable heterostructures containing Bi in the top layer. After removing the native oxide from the InAs or GaAs surface, Bi is deposited onto the substrate either at

room or elevated sample temperature in a sequential manner. The Knutsson cell evaporator containing pieces of Bi was heated to a temperature of 400°C, if not stated otherwise. As a final fabrication step, several annealing steps were carried out up to a substrate temperature of 400°C. Characterization was carried out after each process step to follow the evolution of Bi induced changes.

In contrast to MBE or MOVPE processes where axial heterostructures can be manufactured for low-dimensional materials like nanowires, our method allows exclusively for the fabrication of radial heterostructures also called core-shell structures. We investigate this in the case of InAs nanosheets.

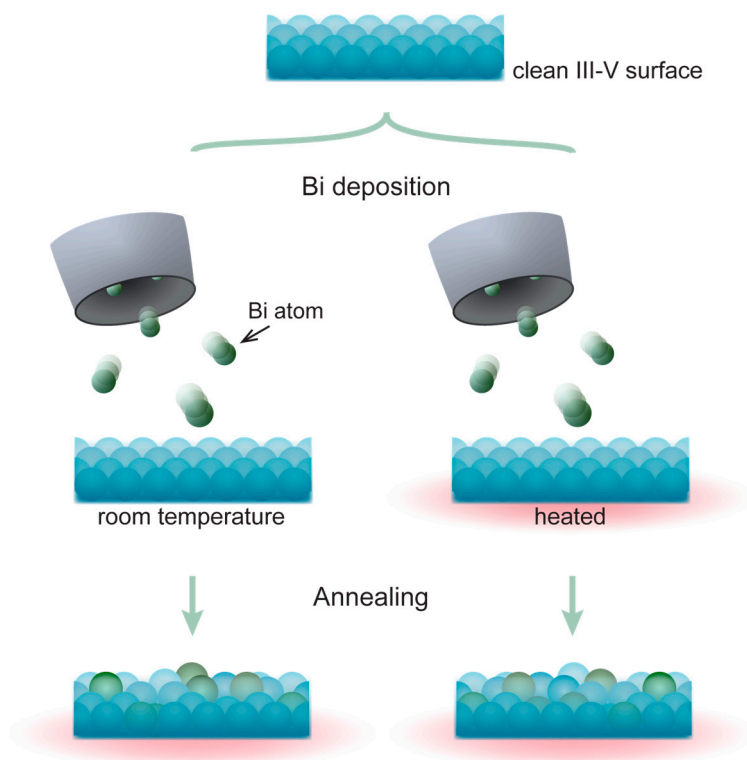


Figure 4.6 Sketch of the two synthesis routes explored in the sections below. After removing the native oxide, Bi atoms are evaporated onto the III-V surface at room temperature (left) or elevated temperature (right). Subsequentlyt the samples are annealed, respectively. This figure is adapted from ¹⁴⁰ (paper III) with permission from the Royal Society of Chemistry.

In the following, we will venture into the cave of surface manipulation via Bi deposition with our GaAs and InAs substrates. I will shine some light onto the structural, chemical, and electronic landscape unfolding ahead of us. It is important to note that each path unwinding in front has specific process parameters and fabrication sequences not necessarily identical to the neighboring one. The details will be indicated at each stage.

Structural changes

Bi on GaAs(111)B

As described in **paper II**, the deposition of Bi on cleaned GaAs(111)B can induce a uniform honeycomb-like structure. Depositing more than a ML of Bi onto this sample while heating to 250°C results in a uniform overlayer with a $\sqrt{3} \times \sqrt{3}$ 30° reconstruction. Here, Bi atoms form covalent bonds downward to the surface instead of occupying substrate lattice positions. Interestingly, a full layer of adatoms corresponds only to a 67% coverage of the GaAs surface. This is a result of a missing atom inside each honeycomb ring. The established 2D layer was found to range over several millimeters. Subsequent annealing to 400°C for about 10 min breaks this pattern as can be seen in figure 4.7 and was measured via low temperature STM. The Bi coverage reduces to about 38% and two distinct regions emerge on the sample: (i) the honeycomb structure observed before, and (ii) areas with single, seemingly randomly distributed Bi atoms. Density functional theory (DFT) calculations confirmed that the most stable position of Bi adatoms is directly on top of an As surface atom. This explains why single atoms are found on the surface instead of clusters. For the latter case, Bi atoms would need to occupy a variety of rather unfavorable positions on the surface in order to bond with each other. The adatom density in these areas is about 1 atom/nm². Additionally, it is obvious that vacancies are present inside the honeycomb structure indicating the starting point of decomposition. Therefore, it is obvious that further annealing led to the complete desorption of all Bi atoms.

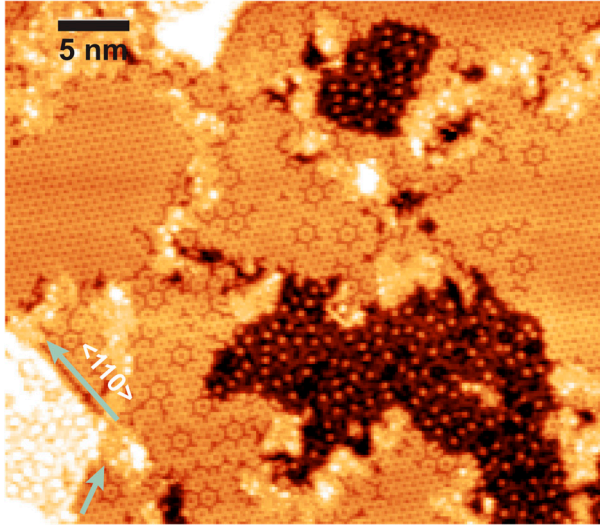


Figure 4.7 STM image of the GaAs(111)B surface after annealing to 400°C. The light green arrows mark the $\langle 110 \rangle$ orientation of the step edges of the upper terrace. Two different areas with Bi atoms are easily distinguishable: (i) the honeycomb structure, and (ii) singled out Bi atoms randomly distributed on the GaAs surface ($I=50$ pA, $V=-3.5$ V). Courtesy of Yi Liu.

Bi on InAs(111)B

For the InAs(111)B surface, we follow the second synthesis branch of Bi deposition at room temperature (RT) and subsequent annealing. Figure 4.8 shows images of the surface after 10 min of RT deposition corresponding to a coverage of about 22%. It is obvious that Bi adatoms tend to form individual clusters rather than a single layer. By measuring the apparent height of the smaller protrusions, we interpret these as single adatoms sitting on top of the InAs surface. Interestingly, the presence of Bi on the surface induces detectable changes in the substrate in the form of meandering grooves. Comparing their depth (indicated in line scan 2 in figure 4.8) to the depth profile of the defects observed after oxide removal excludes the development of additional vacancies in the surface. Since the STM image was taken with high tunneling bias of -3 V, the apparent height is expected to mainly depend on the topography of the surface rather than the LDOS. Therefore, it seems that the interaction of Bi adatoms with the top InAs surface layer induces very locally shifts or reconstructions in the crystal lattice.

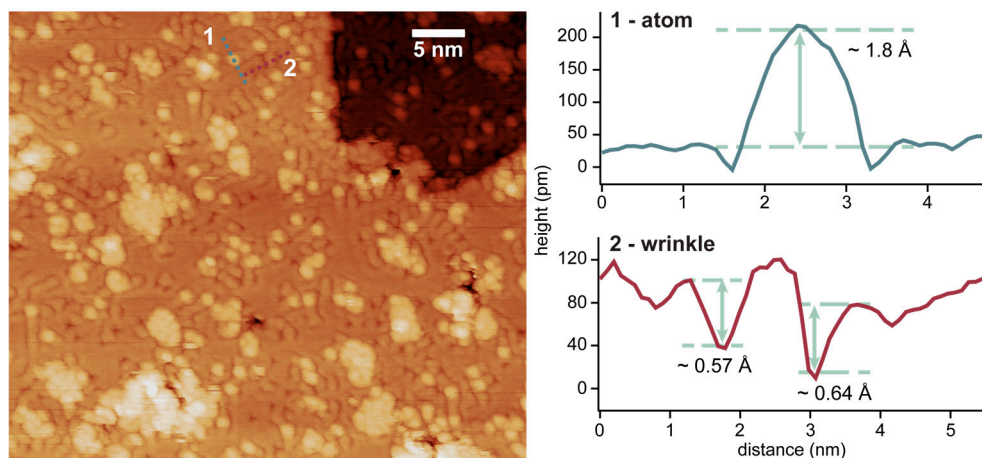


Figure 4.8 Left: STM image of the InAs(111)B surface after depositing Bi at RT ($I=120\text{pA}$, $V=-2.8\text{V}$). Right: line scans of the areas indicated in the STM image. The Bi adatoms are not incorporated into the surface, but rather sit on top.

After annealing the sample to 400°C under Hydrogen pressure and an additional 5 min Bi deposition with the sample at RT, the surface changes dramatically again. This is indicated in figure 4.9. One might say that the surface looks similar compared to the cleaned surface (figure 4.1) with single, small protrusions and a handful of larger clusters. By analyzing the height profile of the single protrusions, it is evident that these atoms are sitting inside the surface layer. Since the atomic structure of the surface is vaguely visible and we do not see any distortion, I anticipate that Bi adatoms substituted substrate atoms in the top layer during the annealing step. Due to the slightly larger atomic size of Bi compared to In and As, incorporated Bi atoms will be detected with a higher contrast in the STM image. Interestingly, the surface wrinkles observed before are not detected anymore. I expect the incorporation of the Bi atoms into the surface lattice to relax the previously induced lattice distortion detected when Bi was adsorbed on top.

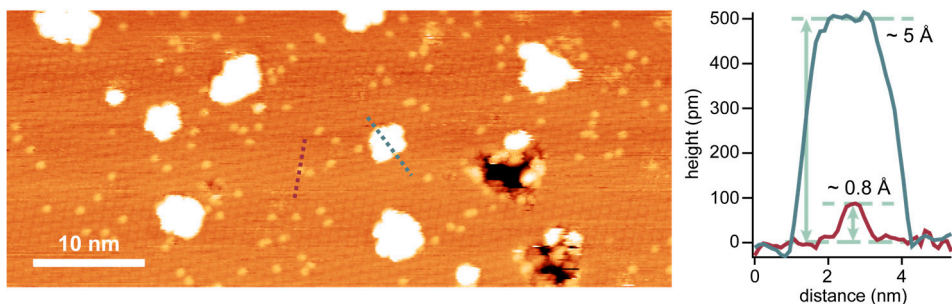


Figure 4.9 Left: STM image of the InAs(111)B surface additional annealing under Hydrogen pressure and Bi deposition at RT ($I=100\text{pA}$, $V=-2.3\text{V}$). The small bright protrusions are single Bi atoms and the larger ones Bi cluster. Right: line scans of the area indicated in the STM image. The height profiles indicate that the single Bi adatoms are incorporated into the surface and the larger clusters accumulate on top.

Noteworthy, the well-organized honeycomb structure detected on GaAs(111)B could not be synthesized on InAs(111)B with the chosen synthesis route. However, leaving the predefined path sometimes leads to hidden places that are hard to reach in a straightforward manner. One of these hidden gems is displayed in figure 4.10. Here, Bi was deposited on to a InAs(111)B sample for 10 min with a sample temperature of 200°C . After investigating the surface via STM, the surface displayed very little adatoms. Therefore, a second deposition step similar to the first one was planned. Seemingly unfortunately, the heater installed on the sample manipulator (required for the same deposition procedure) had some malfunction. This led to a 20 min Bi deposition with the sample being at RT and a subsequent annealing step to about 200°C for 5-10 min carried in a different UHV chamber. As a result, a flower-like pattern appeared on the InAs surface (see figure 4.10). The line profile indicates that this pattern is formed of Bi adatoms on the surface arranging themselves. The height is too little for a monolayer step of InAs(111)B and too large for Bi atoms being incorporated into the surface. On the upper terrace, the smaller white protrusions indicated single Bi atoms sitting on top of the surface similar to the region detected on GaAs(111)B after annealing.

When finding your way through unknown territory you might be too focused on the prior defined goal that you end up losing track of the interesting things around you. This happened to me on my hunt through the nanowire forest to find suitable specimen to scan on. I did not notice the beauty of the underlying InAs(111)B substrate while moving from one wire to the next. The moment I turned around to have a closer look it was too late. The mystic creature had vanished into the woods.

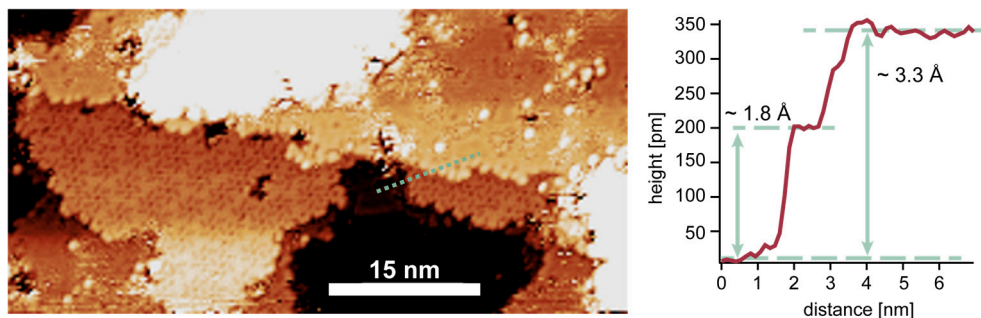


Figure 4.10 Left: STM image of the flower-like, Bi-induced structure found on InAs(111)B. ($I=100$ pA, $V=-3$ V). Right: line scan of the area indicated in the STM. The height profile indicates monolayer sized steps.

Bi on InAs(110)

Moving on to InAs(110) substrates, it is evident that Bi adatoms act differently when engaging with this surface. Here, we observe predominantly the growth of ordered islands compared to the cluster formation on InAs(111)B as can be seen in figure 4.11 and 4.12. In contrast to the protagonists before, InAs(110) surfaces engaged in a multitude of different preparation and characterization scenarios. Two of them I will describe in the following.

We will begin with a native oxide removal on an InAs(110) wafer within an MBE system as described in section 4.1¹⁴. There is extensive study of this surface prepared via cleaving or a sequence of sputter and annealing steps. But a detailed description of the surface quality and morphology for MBE grown substrates is still

¹⁴ These experiments were carried during a stay with Joanna Millunchick's group at the University of Michigan, Ann Arbor.

missing. The cleaned surface in section 4.1 did not show any signs of reconstruction or a significant number of defects. After the growth of additional 200 nm of InAs at about 460°C, the sample was brought to 290°C with an As backpressure which was cut-off at the target value. The InAs surface was exposed to Bismuth atoms for 25 sec with a flux of 5.7×10^{-8} Torr. The corresponding surface investigated with an STM attached to the MBE system is shown in figure 4.11. Due to a malfunction of the software, the overall size of the image is incorrectly saved leading to wrong absolute length values. However, a relative analysis is still possible. In general, two main changes of the surface are visible: (i) brighter, single protrusions on the substrate, and (ii) newly formed islands. I consider (i) as incorporated Bi atoms due to the small height difference of 0.4-0.8 Å from the substrate. For the case (ii), the islands show an elongated shape suggesting a predominant growth direction along the $\langle \bar{1}11 \rangle$ direction. Figure 4.11c indicates that islands with two different heights are present. Line scan 3 in figure 4.11b suggests that the lowest islands consist of one, and the highest of two atomic layers (step size of InAs(110) about 1.9 Å). It is evident that even though Bi incorporation into the InAs surface occurs homogeneously over the whole sample at the start of the deposition, island growth dominates the subsequent incorporation of arriving adatoms. The islands show an increased atomic distance by a factor of ~ 2 compared to the underlying substrate. A (1x2) growth model for Bi incorporation in InAs(110) was already proposed by Betti et al.⁵⁴. However, as discussed in the supplementary information of **paper III**, we do not agree completely with the proposed model. Based on our XPS investigation explained in the next section, we suggest a different incorporation scenario in which Bi atoms pull out In atoms to be incorporated into the surface.

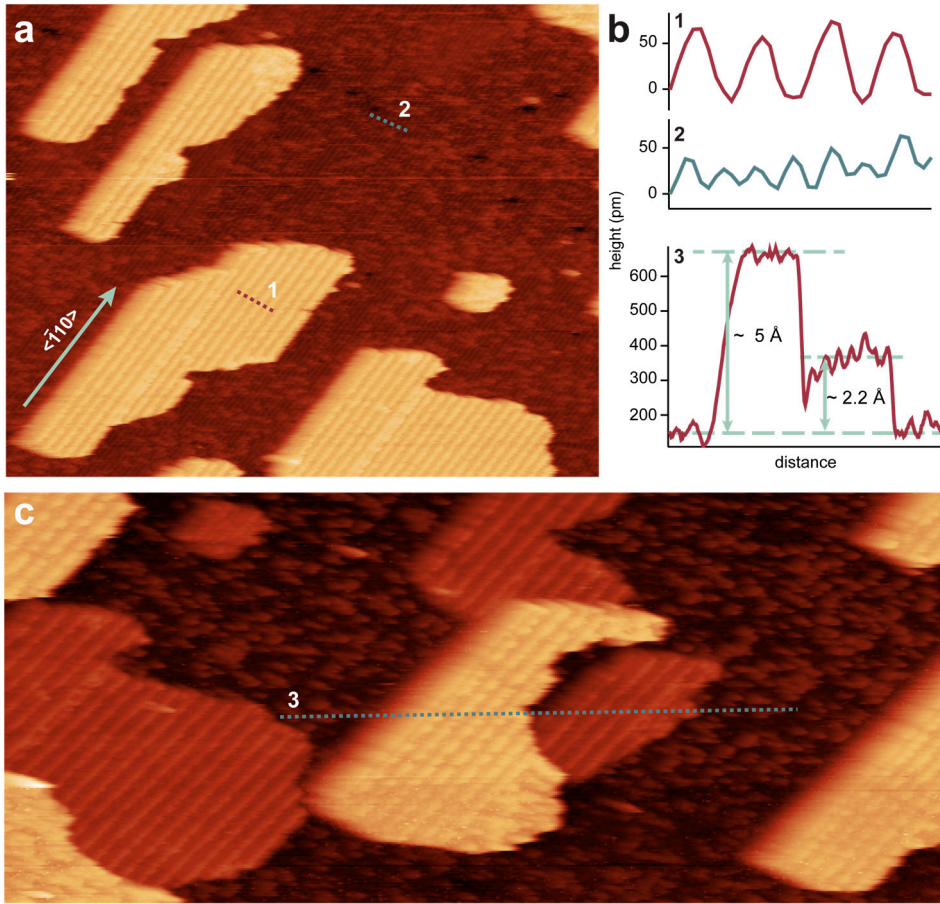


Figure 4.11 STM images of the InAs(110) after depositing Bi at elevated sample temperature in an MBE system. Due to a malfunction in the software the length scale is not reliable. However, comparing line scan 1 and 2, it is evident that the islands exhibit a larger atomic distance. Additionally, the predominant island growth direction is indicated in (a). (c) Exemplifies that islands with different heights are present on the surface (both images taken with $I=88.5$ pA, $V=-2.9$ V).

Interestingly, when following the deposition path at room temperature, a quite different scenario emerges. The InAs(110) surface shown in figure 4.12 was manipulated in our UHV system via Hydrogen cleaning and subsequent Bi evaporation for 20 min. Although the deposition time is significantly longer compared to the deposition in the MBE system, we also do not observe full coverage. This is a result of a lower temperature chosen for the Bi evaporator. A subsequent smaller Bi flux enables a higher control of adatom interaction with the surface.

Interestingly, no predominant growth direction of the formed islands is visible. Instead, a rectangular pattern can be detected on the islands rotated by about 34° with respect to the underlying substrate. This pattern has a periodicity of around 1.3 nm in one and 1.8 nm the other direction, as well as a step height of 2.2 Å. It corresponds well to a single layer of Bi adatoms with an increased and rotated unit cell compared to the InAs(110) surface. The influence of the underlying crystal structure is quite stunning when comparing both room temperature depositions on InAs(111)B (figure 4.8) and InAs(110) (figure 4.12). Bi atoms seem to favor the structure of the non-polar InAs(110) surface for the synthesis of ordered layers. The cluster formation on InAs(111)B implies that As-Bi interaction is less favorable than Bi-Bi interaction. This is in strong contrast to the GaAs(111)B surface presented above and in **paper II**.

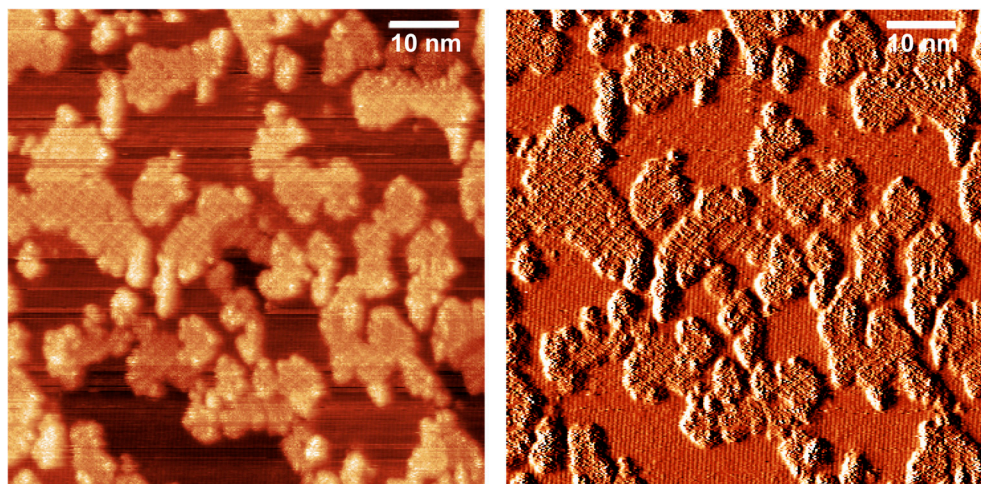


Figure 4.12 STM image of the InAs(110) after RT deposition of Bi. The right side shows the derivative of the image along the x-direction to signify the rectangular pattern in the islands compared to the atomic lines of the substrate ($I=30$ pA, $V=-3$ V). Courtesy of Tobias Alpskog.

Chemical fingerprint

We have followed our main characters into the cave of surface alteration, where each one of them started to develop a new skin. Depending on the environment they encountered, different textures emerged providing each heroine with unique features. In small groups they venture further out into the dark. The experiences of one of the groups in the grotto of chemical scrutiny will be told in the following.

GaAs(111)B

Paper II describes in detail the bonding mechanism behind the Bi induced honeycomb structure illustrated in section 4.3. It was possible to show that Bi bonds solely to the As atoms of the GaAs(111)B surface layer by analyzing the Bi 5d core level. Interestingly, the distance between individual adatoms is too large for Bi-Bi bonds to form. This is confirmed by DFT calculations. Bi-Bi bonds were only observed after additional deposition with the sample at RT. The underlying ordered honeycomb structure is not continued in vertical direction since Bi atoms start to agglomerate in clusters. This metallic Bi is not stable at higher temperatures and partly disintegrates already at an annealing temperature of 250°C. On the other hand, As-Bi bonds persevere even at sample temperatures around 400°C. This is a strong indication for covalent bonding between the substrate As and Bi adatom. However, the formation of metallic Bi clusters gives rise to an additional component between the As-Bi and Bi-Bi bonding component in the Bi 5d core level spectrum. This is a result of weakened polar As-Bi bonds induced by additional Bi atoms on top of the original Bi honeycomb layer. There is no indication of Ga-Bi bonds after any process step.

InAs(110)

In **paper III**, both synthesis routes depicted in figure 4.6 were pursued. In contrast to the GaAs(111)B surface, InAs(110) exhibits both (group III and V) elements in the surface layer with dangling bonds. As a result, we clearly observe In-Bi bonds in the Bi 4f (see figure 4.13 for a selection) and the In 4d core level spectrum for each process step. This is very interesting, since the Bi-V bonds are almost neglectable except for the amount of metallic Bi forming during RT deposition steps. In-Bi bonds are even present on the surface after annealing to 400°C. This is in clear contrast to theoretical calculations showing that As-Bi bonds should be more temperature resilient compared to In-Bi bonds ¹⁴¹.

Analyzing the XPS results at RT, it is obvious that the formed islands exhibit a variety of different bonds. The number of Bi atoms bonding to As or In surface atoms is similar for the first deposition as indicated in figure 4.13a. However, $\frac{2}{3}$ of the arriving adatoms contribute to the metallic Bi component. Considering the STM data presented above, the periodicity in the newly formed islands is larger than 1 nm in both directions. This distance would exclude Bi-Bi bonds. Therefore, within this 1.3 nm x 1.8 nm ‘unit cell’ additional Bi atoms need to be present solely bonding within the same layer and not to the substrate. I can exclude the formation of Bi cluster on top of single Bi atoms bonding with the InAs surface due to the low step height detected for all structures in section 4.1. Interestingly, for the following deposition steps an intensity increase is only observed for In-Bi and Bi-Bi bonds. An overall coverage of about two ML is detected after the final deposition. Here, about 42% of the Bi 4f core level intensity is attributed to In-Bi bonds. This suggests a subsequent change within the atomic structure of the island to account of the observed ratio between metallic Bi and In-Bi bonds.

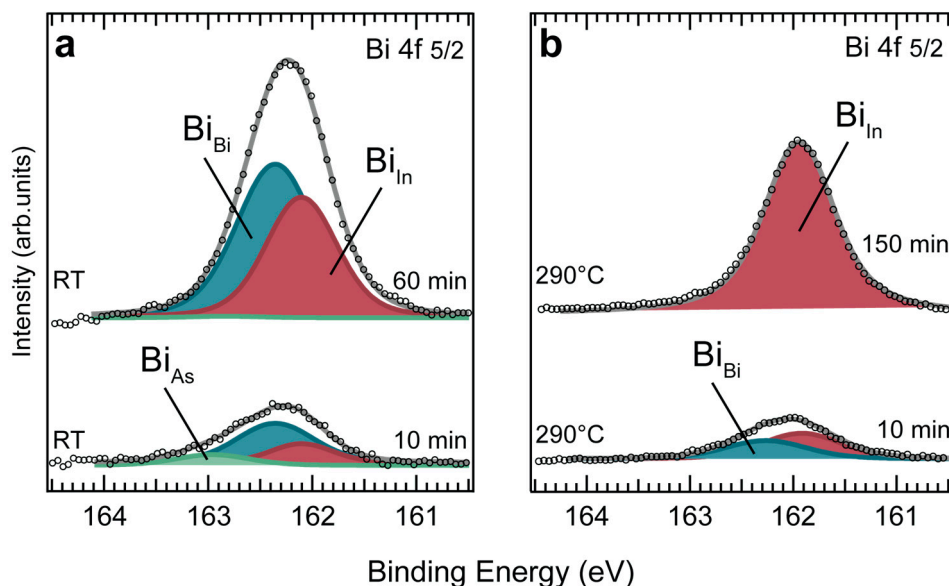


Figure 4.13 XP spectra of the Bi 4f 5/2 core level after different deposition steps on an InAs(110) surface: (a) with the sample at RT and (b) the sample at 290°C. The time indicated at each spectrum indicates the overall time the sample was exposed to the Bi evaporator. The figure is adapted from ¹⁴⁰ (ref (paper III)) with permission from the Royal Society of Chemistry.

The STM images of the InAs(110) surface, after depositing Bi at elevated sample temperature, indicates a (1x2) reconstruction of the implemented overlayer. Betti et. al ⁵⁴ suggested a (1x2) missing row reconstruction based on a variety of diffraction experiments and theoretical calculations were incorporated Bi atoms exhibit bonds to As, In and Bi atoms, respectively¹⁵. Accordingly, we should detect three different components in the Bi 4f core level spectra. As can be seen from figure 4.13b, this is not applicable in our case. Furthermore, for extended deposition times only In-Bi bonds are detected. Therefore, we propose a different structural model in the supplementary information of **paper III** where In atoms are pulled out of the surface and reincorporated into the growing islands. Unfortunately, XPS studies based on the sample preparation process used in ⁵⁴ are not available.

¹⁵ The InAs(110) surface was prepared via a sequence of sputtering and annealing, followed by RT deposition of several MLs of Bi and subsequent annealing. Sharp (1x2) diffraction spots were detected at 480K.

InAs(11 $\bar{2}$ 0)

InAs(11 $\bar{2}$ 0) is like InAs(110) a non-polar surface with In and As atoms in the top layer. As shown in figure 2.1, both surfaces exhibit the same nearest neighbor configuration. Nevertheless, when performing the same experimental sequence very distinct differences arise in the Bi 4f core level spectra as depicted in figure 4.14 and in detail discussed in **paper III**. First, a significant increase of metallic Bi is observed for both synthesis routes during each deposition sequence. Secondly, we do not see any In-Bi bond formation for depositions carried out at room temperature. And finally, all Bi atoms desorb completely from the surface when annealing the sample to 400°C.

The steady increase of Bi-Bi bonds in the respective deposition scheme indicates a self-limiting interaction of the arriving Bi atoms with the InAs surface. For the first RT deposition, Bi atoms favor on top positions close to As surface atoms, as can be seen in figure 4.14a and is in agreement with DFT calculations. Subsequently, cluster formation and island growth become more favorable. Depositing at elevated sample temperature facilitates the integration of Bi atoms on As lattice positions in the top layer forming In-Bi bonds (see figure 4.14b) with subsequent Bi-Bi formation. This is in contrast to the InAs(110) facet, where the large amount of In-Bi bonds suggests interaction of adatoms beyond the outermost substrate layer. Annealing the sample results in an increase of In-Bi bonds and the subsequent retrieval of the pristine InAs(11 $\bar{2}$ 0) surface at 400°C for both synthesis routes.

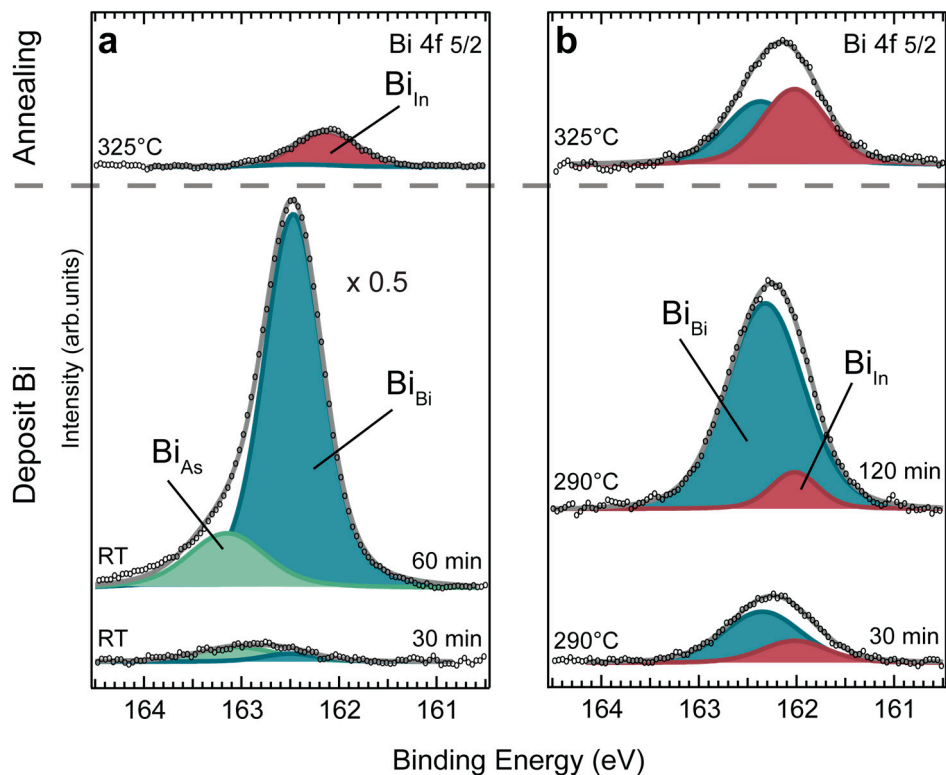


Figure 4.14 XP spectra of the Bi 4f 5/2 core level after different deposition steps on an InAs(11 $\bar{2}$ 0) surface: (a) with the sample at RT and (b) the sample at 290°C. The time indicated at each spectrum indicates the overall time the sample was exposed to the Bi evaporator. The top spectrum are 10 min annealing steps, respectively. The figure is adapted from ¹⁴⁰ (paper III) with permission from the Royal Society of Chemistry.

Electronic changes

From the large number of III-V heroines setting out to seek adventures in the cave of surface manipulation just a few managed to endure the scrutiny of the chemical grotto. Only the InAs WZ nanosheets, brave enough to move on, continued to explore the neighboring chamber of electronic revelation. But what a surprise, another passage leads into the chamber! And a slightly familiar figure walks through with a skin never seen before. The story on how the chamber uncovered both heroines' secrets buried deepest within them, will be the last one told in this book.

InAs(11 $\bar{2}$ 0)

As the WZ crystal structure of InAs can only be fabricated in low dimensional material, experimental data on the band structure is still missing. However, a growing number of ARPES beamlines is dedicated to focus on the micro- or nanometer size range. Aside from the high competition for beamtimes, there are several drawbacks for these specialized setups, e.g. long acquisition time (= sample exposure) due to a low signal intensity and X-ray flux, as well as a limited range of available photon energies^{142–144}. In **paper IV**, we demonstrate that a specific part of the band structure of InAs(11 $\bar{2}$ 0) nanosheets can be accessed via averaging ARPES setups. Due to the 2D like shape of the nanosheets, the majority display the same crystal facet towards the X-ray beam and analyzer after transfer to the measurement sample. This allows for band structure measurements over many specimens. However, due to the random rotation around their normal axis, the signal blurs for $k_{||} > 0$. Figure 4.15 shows the first Brillouin zones for a hexagonal crystal lattice and the accessible symmetry points in the neighboring zones for photon energy scans in normal emission for the (11 $\bar{2}$ 0) surface.

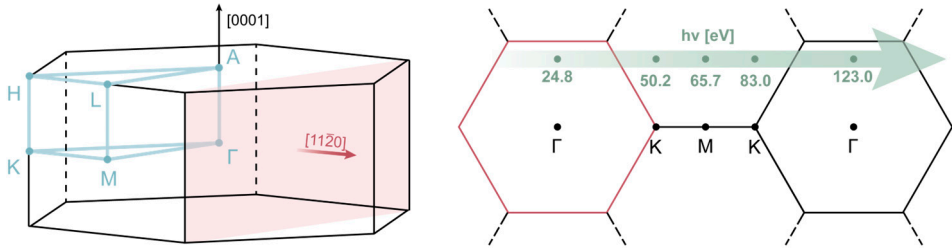


Figure 4.15 Brillouin zone of the hexagonal lattice and its respective symmetry points. The direction of the $(11\bar{2}0)$ surface is indicated in the left image. By changing the photon energy, different symmetry points in adjacent Brillouin zones along the surface normal become accessible as depicted on the right side (red lines mark the first Brillouin zone). The energy values are estimated with free electron final state approximation (see the supplemetray information of **paper IV**) for each symmetry point.

As described in **paper IV**, we show that changes at the Γ -point induced by Bi deposition are detectable. Here, the VB shifts upwards in contrast to bands at the M-symmetry point which stay localized. Interestingly, the InAs WZ $(11\bar{2}0)$ crystal structure displays an electron pocket after removal of the native oxide. This is in contrast to the InAs(110) surface, where 2DEGs only appear after metal deposition¹⁴⁵. We attribute the 2DEG to a specific step and edge morphology which is altered by the arriving adatoms in consistency with our XPS experiments for depositions at elevated sample temperatures.

InAs(111)B with As overlayer

For **paper V** a different synthesis route was taken. An InAs(111)B wafer was deoxidized in an MBE system with an As flux of 1.2×10^{-5} Torr at a temperature of 450°C. After the native oxide removal, the sample temperature was lowered to 100°C for Bi deposition of less than a ML. Subsequently, an amorphous As overlayer of 20 nm was grown at 5°C in order to protect the InAs:Bi:As interface. Single pieces of the substrate were introduced into two ARPES setups combined with LEED and preparation chamber. Here, the substrates were sputtered for 10-15 min under an 45° angle between sputter gun and surface with 5×10^{-6} mbar Ar. Subsequent annealing to temperatures around 200-300°C, allowed for a slow removal of the As overlayer and prohibited desorption of the Bi atoms. The

difference in the band structure between a pristine InAs(111)B surface and our sample after removing part of the As overlayer are shown in figure 4.16.

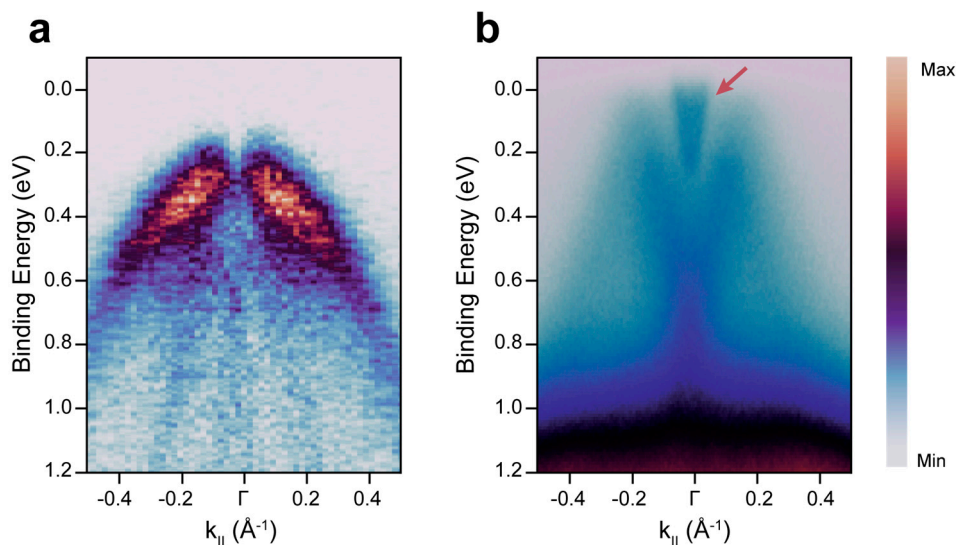


Figure 4.16 ARPES spectra of the (a) pristine InAs(111)B surface, and (b) of a sample exposed to Bi and As deposition after decreasing the overlayer thickness. The presence of an electron pocket is indicated by the red arrow and new bands can be observed resembling an M-shape.

Several XPS and ARPES data points were collected for varying As overlayer thicknesses ranging from 0-10 nm. By comparison, it is found that the VB of the InAs substrates shifts downwards by ~ 400 meV and an electron pocket forms (indicated by the red arrow in figure 4.16b). This is still present after complete desorption of the excess As and therefore attributed to n-type doping of the substrate induced by Bi atoms. Furthermore, a clear dependency between the additional bands, faint M-shape in figure 4.16b, and the presence of a well-ordered interface between the InAs substrate and the overlayer is detected. DFT calculations confirm the origin of the new electronic states due to the formation of a 2D unreconstructed BiAs layer protected by the excess As on top.

5 Outlook

This is the end of the adventures of III-V surfaces described in this book. With our protagonists, we ventured into the unknown and saw how different methods of skin cleansing were performed to prepare them for the upcoming events. During the first endeavor, our InAs heroin discovered metal ornaments that can help to prevent drops of sweat forming when the outer temperature rises. The second big challenge brought a collection of III-V characters into a cave system, where they were accessorized with a new skin. This new surface was individually fitted in composition and arrangement dependent on the owner and we got hold of a glimpse of its potential properties in the chamber of electronic revelation. Naturally, the question of what lies ahead is sneaking into the field of view...

Since the detected effect of droplet inhibition on InAs(111)B substrates via Al/Pd metal stacks is robust against surface defects, lithographic process, as well as metal pattern size and shape, we are confident that it is applicable to other III-V semiconductors like GaAs, InSb, InP etc. (as mentioned before). A wider proof-of-concept study with a variety of substrate types and different metals would be very interesting. Based on the binary phase diagrams of Au^{120,121}, Ti^{119,122} and Pt¹²³, Ga and In droplets should not form close to the metal stack.

With the setup used in this study, the temperature threshold of 650°C is induced by the high diffusion coefficient of In atoms on the InAs surface. The employed heating and cooling rates are too slow enabling a large amount of newly released In atoms from the same surface area to migrate towards the metal stack. As a result, a single InAs surface area is contributing with numerous In atoms to the In concentration in the Pd layer exceeding its solubility limit fast. Therefore, it would be interesting to investigate the effect of faster temperature ramps. Here, a single InAs surface area should release a lower amount of In atoms. Thus, In atoms from

a wider surface region can alloy into the metal before the up-take limit is reached. This could increase the size of the droplet-free zone further.

One goal of the beamtime conducted at MaxPEEM was to study the dynamics of droplet formation and movement especially at the boundary of droplet and droplet-free zone by recording a movie while annealing the sample. Due to several technical problems, only a single region at the edge of the metal stack could be measured. The results are shown and discussed in **paper I**. Therefore, more in-depth studies of the droplet dynamics at various distances with respect to the metal contacts could be useful to utilize the describe effect to the full extent.

As the benefit of the described phenomena is aimed towards device fabrication techniques, implementing our findings into a whole manufacturing sequence would be very exciting. Since larger temperature ranges are accessible, it would be interesting to see whether new materials can be combined on top of each other for the following fabrication steps and devices built upon the III-V layer.

As for the Bi incorporation into III-V surfaces, our simplified approach of depositing pure elements and annealing the sample should be applicable to other materials and substrate types. I have carried out similar studies on InSb nanosheets with Bi via XPEEM and observed distinct changes in the Sb and In 4d core level peaks. However, the observed behavior seems very complex and additional experiments with, e.g. STM would be useful to interpret the results.

Additional STM measurements would also clarify the morphological changes induced by the different process parameters observed in **paper III** for InAs(11 $\bar{2}$ 0) nanosheets. The STM data I gathered was usually convoluted by tip induced effects and atomic resolution was only partly achievable. However, hints of an ordered incorporation comparable to Bi incorporation into GaAs WZ segments⁴⁴ are detectable as shown in figure 3.3. This could be combined with electrical device characterization and scanning tunnelling spectroscopy¹⁴⁶ to determine changes in the electronic properties of the nanosheets induced by Bi substitution of As surface atoms.

In general, moving on from structural and chemical investigations towards determining the electronic changes induced by Bi incorporation is next in line. As we have seen, all III-V crystal facets displayed ordered atomic arrangements after

specific process sequences promising alterations in the band structure of the pristine material. This, however, is not a trivial task. E.g. for the Bi-induced honeycomb structure on GaAs(111)B, several attempts to recreate the overlayer at an ARPES beamtime failed due to setup differences and contamination of a preparation chamber. However, experiments involving a vacuum suitcase, our preparation chamber and the BLOCH beamline at Max IV might enable these measurements and facilitate a higher turnover between successful sample preparation and ARPES measurements.

References

- (1) Bardeen, J.; Brattain, W. H. Transistor, a Semiconductor Triode. *Phys. Rev.* **1948**, *74* (230), 230–231.
- (2) Brattain, W. H.; Bardeen, J. Nature of the Forward Current in Germanium Point Contacts. *Phys. Rev.* **1948**, *74* (231), 231–232.
- (3) Shockley, W.; Pearson, G. L. Modulation of Conductance of Thin Films of Semiconductors by Surface Charges. *Phys. Rev.* **1948**, *74* (2), 232–233.
- (4) Bardeen, J.; Brattain, W. H. Physical Principles Involved in Transistor Action. *Phys. Rev.* **1949**, *75* (8), 1208–1226.
- (5) Welker, H. Über Neue Halbleitende Verbindungen. *Zeitschrift für Naturforsch. A* **1952**, *7* (1), 744–749.
- (6) Ivanov, S. Remembering Zhores Alferov. *Nat. Photonics* **2019**, *13*, 657–659.
- (7) Folberth, O. G.; Weiß, H. Herstellung Und Elektrische Eigenschaften von InP Und GaAs. *Zeitschrift für Naturforsch. A* **1955**, *10* (8), 615–619.
- (8) Welker, H. Über Neue Halbleitende Verbindungen II. *Zeitschrift für Naturforsch. A* **1953**, *8* (4), 248–251.
- (9) Talley, R. M.; Enright, D. P. Photovoltaic Effect in InAs. *Phys. Rev.* **1954**, *95* (4), 1092–1094.
- (10) Folberth, O. G.; Madelung, O.; Weiß, H. Die Elektrischen Eigenschaften von Indiumarsenid II. *Zeitschrift für Naturforsch. A* **1954**, *9* (11).
- (11) Folberth, O. G.; Grimm, R.; Weiß, H. Über Die Elektrischen Eigenschaften von InAs. *Zeitschrift für Naturforsch. A* **1953**, *8* (12), 826.
- (12) Cunnell, F. A.; Saker, E. W.; Edmond, J. T. A Note on the Semiconducting Compound InSb. *Proc. Phys. Soc. B* **1953**, *66* (1115).
- (13) Pearson, G. L.; Tanenbaum, M. The Magnetoresistance Effect in InSb. *Phys. Rev.* **1953**, *90* (153).
- (14) Tanenbaum, M.; Maita, J. P. Hall Effect and Conductivity of InSb Single Crystals. *Phys. Rev.* **1953**, *91* (1009).
- (15) Rode, D. L. Electron Mobility in Direct-Gap Polar Semiconductors. *Phys. Rev. B* **1970**, *2* (4), 1012–1024.
- (16) Neamen, D. A. *Semiconductor Physics and Devices*, 4th ed.; McGraw-Hill: New York, 2012.
- (17) Del Alamo, J. A. Nanometre-Scale Electronics with III-V Compound Semiconductors. *Nature* **2011**, *479*, 317–323.

- (18) Schaller, R. R. Moore's Law: Past, Present and Future. *IEEE Spectr.* **1997**, *34* (6), 52–59.
- (19) Fan Wu, He Tian, Yang Shen, Zhan Hou, Jie Ren, Guangyang Gou, Yabin Sun, Y. Y. & T.-L. R. Vertical MoS₂ Transistors with Sub-1-Nm Gate Lengths. *Nature* **2022**, *603*, 259–264.
- (20) Quhe, R.; Liu, J.; Wu, J.; Yang, J.; Wang, Y.; Li, Q.; Li, T.; Guo, Y.; Yang, J.; Peng, H.; Lei, M.; Lu, J. High-Performance Sub-10 Nm Monolayer Bi₂O₂Se Transistors. *Nanoscale* **2019**, *11*, 532–540.
- (21) Grange, J. D.; Parker, E. H. C.; King, R. M. Relationship of MBE Growth Parameters with the Electrical Properties of Thin (100) InAs Epilayers. *J. Phys. D. Appl. Phys.* **1979**, *12*, 1601.
- (22) Bracker, A. S.; Yang, M. J.; Bennett, B. R.; Culbertson, J. C.; Moore, W. J. Surface Reconstruction Phase Diagrams for InAs, AlSb, and GaSb. *J. Cryst. Growth* **2000**, *220* (4), 384–392.
- (23) Liu, W. K.; Santos, M. B. Surface Reconstructions of InSb(001) during Molecular Beam Epitaxy. *Surf. Sci.* **1994**, *319* (1), 172–183.
- (24) AbuWaar, Z. Y.; Wang, Z. M.; Lee, J. H.; Salamo, G. J. Observation of Ga Droplet Formation on (311)A and (511)A GaAs Surfaces. *Nanotechnology* **2006**, *17* (16), 4037–4040.
- (25) Reyes, K.; Smereka, P.; Nothorn, D.; Millunchick, J. M.; Bietti, S.; Somaschini, C.; Sanguinetti, S.; Frigeri, C. Unified Model of Droplet Epitaxy for Compound Semiconductor Nanostructures: Experiments and Theory. *Phys. Rev. B* **2013**, *87* (16), 165406.
- (26) Kim, J. S. Ga-Migration on a Ga-Rich and As-Stabilized Surfaces: Ga-Droplet and GaAs- Nanostructure Formation. *Mater. Sci. Semicond. Process.* **2017**, *57*, 70–76.
- (27) Tersoff, J.; Jesson, D. E.; Tang, W. X. Running Droplets of Gallium from Evaporation of Gallium Arsenide. *Science* (80-.). **2009**, *324* (236).
- (28) Kanjanachuchai, S.; Photongkam, P. Dislocation-Guided Self-Running Droplets. *Cryst. Growth Des.* **2015**, *15* (1), 14–19.
- (29) Kanjanachuchai, S.; Euaruksakul, C. Self-Running Ga Droplets on GaAs (111)A and (111)B Surfaces. *ACS Appl. Mater. Interfaces* **2013**, *5*, 7709–7713.
- (30) Lee, J. W.; Jang, D.; Mouis, M.; Kim, G. T.; Chiarella, T.; Hoffmann, T.; Ghibaudo, G. Mobility Analysis of Surface Roughness Scattering in FinFET Devices. *Solid. State. Electron.* **2011**, *62* (1), 195–201.
- (31) Hyun Kum, Doeon Lee, Wei Kong, Hyunseok Kim, Yongmo Park, Yunjo Kim, Yongmin Baek, Sang-Hoon Bae, K. L. & J. K. Epitaxial Growth and Layer-Transfer Techniques for Heterogeneous Integration of Materials for Electronic and Photonic Devices. *Nat. Electron.* **2019**, *2*, 439–450.
- (32) Bouarissa, N.; Boucenna, M. Band Parameters for AlAs, InAs and Their Ternary Mixed Crystals. *Phys. Scr.* **2009**, *79* (015701).

- (33) Polak, M. P.; Scharoch, P.; Kudrawiec, R. First-Principles Calculations of Bismuth Induced Changes in the Band Structure of Dilute Ga-V-Bi and In-V-Bi Alloys: Chemical Trends versus Experimental Data. *Semicond. Sci. Technol.* **2015**, *30* (9), 094001.
- (34) Linhart, W. M.; Kudrawiec, R. Temperature Dependence of Band Gaps in Dilute Bismides. *Semicond. Sci. Technol.* **2018**, *33* (073001).
- (35) Bouarissa, N.; Aourag, H. Effective Masses of Electrons and Heavy Holes in InAs, InSb, GaSb, GaAs and Some of Their Ternary Compounds. *Infrared Phys. Technol.* **1999**, *40* (4), 343–349.
- (36) Balanta, M. A. G.; Kopaczek, J.; Orsi Gordo, V.; Santos, B. H. B.; Rodrigues, A. D.; Galeti, H. V. A.; Richards, R. D.; Bastiman, F.; David, J. P. R.; Kudrawiec, R.; Galvao Gobato, Y. Optical and Spin Properties of Localized and Free Excitons in GaBixAs1-x/GaAs Multiple Quantum Wells. *J. Phys. D. Appl. Phys.* **2016**, *49* (355104).
- (37) Webster, P. T.; Shalindar, A. J.; Riordan, N. A.; Gogineni, C.; Liang, H.; Sharma, A. R.; Johnson, S. R. Optical Properties of InAsBi and Optimal Designs of Lattice-Matched and Strain-Balanced III-V Semiconductor Superlattices. *J. Appl. Phys.* **2016**, *119* (225701).
- (38) Dutta, P. S. Bulk Crystal Growth of Ternary III-V Semiconductors. In *Springer Handbook of Crystal Growth*; Dhanaraj, G., Byrappa, K., Prasad, V., Dudley, M., Eds.; Springer Berlin Heidelberg: Berlin, Heidelberg, 2010; pp 281–325.
- (39) Wang, L.; Zhang, L.; Yue, L.; Liang, D.; Chen, X.; Li, Y.; Lu, P.; Shao, J.; Wang, S. Novel Dilute Bismide, Epitaxy, Physical Properties and Device Application. *Crystals* **2017**, *7* (3), 63.
- (40) Guan, Y.; Forghani, K.; Kim, H.; Babcock, S. E.; Mawst, L. J.; Kuech, T. F. Surface Kinetics Study of Metal–Organic Vapor Phase Epitaxy of GaAs1-yBi_y on Offcut and Mesa-Patterned GaAs Substrates. *J. Cryst. Growth* **2017**, *464*, 39–48.
- (41) Zaied, I.; Fitouri, H.; Chine, Z.; Rebey, A.; El Jani, B. Atmospheric-Pressure Metal–Organic Vapor-Phase Epitaxy of GaAsBi Alloys on High-Index GaAs Substrates. *J. Phys. Chem. Solids* **2014**, *75* (2), 244–251.
- (42) Lewis, R. B.; Masnadi-Shirazi, M.; Tiedje, T. Growth of High Bi Concentration GaAs 1-XBi_x by Molecular Beam Epitaxy. *Appl. Phys. Lett.* **2012**, *101* (082112), 1–5.
- (43) Hjort, M.; Kratzer, P.; Lehmann, S.; Patel, S. J.; Dick, K. A.; Palmstrøm, C. J.; Timm, R.; Mikkelsen, A. Crystal Structure Induced Preferential Surface Alloying of Sb on Wurtzite/Zinc Blende GaAs Nanowires. *Nano Lett.* **2017**, *17*, 3634–3640.
- (44) Liu, Y.; Knutsson, J.; Wilson, N.; Young, E.; Lehmann, S.; Dick, K. A.; Palmstrøm, C. J.; Mikkelsen, A.; Timm, R. Self-Selective Formation of Ordered 1D and 2D GaBi Structures on Wurtzite GaAs Nanowire Surfaces. *Nat. Commun.* **2021**, *12* (5990).
- (45) Wassermeier, M.; Sudijono, J.; Johnson, M. D.; Leung, K. T.; Orr, B. G.; Däweritz, L.; Ploog, K. Reconstruction of the GaAs (311)A Surface. *Phys. Rev. B* **1995**, *51* (20), 14721–14724.

- (46) Neave, J. H.; Joyce, B. A.; Dobson, P. J.; Norton, N. Dynamics of Film Growth of GaAs by MBE from Rheed Observations. *Appl. Phys. A* **1983**, *31*, 1–8.
- (47) Haberern, K. W.; Pashley, M. D. GaAs(111)A-(2 X 2) Reconstruction Studied by Scanning Tunneling Microscopy. *Phys. Rev. B* **1990**, *41* (5).
- (48) Rosini, M.; Righi, M. C.; Kratzer, P.; Magri, R. Indium Surface Diffusion on InAs (2×4) Reconstructed Wetting Layers on GaAs(001). *Phys. Rev. B* **2009**, *79* (075302).
- (49) Snyder, C. W.; Sudijono, J.; Larn, C.-H.; Johnson, M. D.; Qrr, B. G. Surface Transformations on Annealed GaAs(001). *Phys. Rev. B* **1994**, *50* (24).
- (50) Taguchi, A.; Kanisawa, K. Stable Reconstruction and Adsorbates of InAs (111)A Surface. *Appl. Surf. Sci.* **2006**, *252*, 5263–5266.
- (51) King, P. D. C.; Veal, T. D.; McConville, C. F.; Zúñiga-Pérez, J.; Muñoz-Sanjosé, V.; Hopkinson, M.; Rienks, E. D. L.; Jensen, M. F.; Hofmann, P. Surface Band-Gap Narrowing in Quantized Electron Accumulation Layers. *Phys. Rev. Lett.* **2010**, *104* (256803), 1–4.
- (52) Bastiman, F.; Cullis, A. G.; David, J. P. R.; Sweeney, S. J. Bi Incorporation in GaAs(100)-2×1 and 4×3 Reconstructions Investigated by RHEED and STM. *J. Cryst. Growth* **2012**, *341* (1), 19–23.
- (53) Ohtake, A.; Ito, T. A. T. As-Rich (2 × 2) Surface Reconstruction on GaAs(111)A. *Surf. Sci.* **2012**, *606*, 1864–1870.
- (54) Betti, M. G.; Berselli, D.; Mariani, C. (1x2) Bi Chain Reconstruction on the InAs(110) Surface. *Phys. Rev. B* **1999**, *59* (24), 760–765.
- (55) Maeda, F.; Watanabe, Y.; Oshima, M. Sb-Induced Surface Reconstruction on GaAs(001). *Phys. Rev. B* **1993**, *48* (19), 14733–14736.
- (56) Nakamura, M.; Fujioka, H.; Ono, K.; Takeuchi, M.; Mitsui, T.; Oshima, M. Molecular Dynamics Simulation of III–V Compound Semiconductor Growth with MBE. *J. Cryst. Growth* **2000**, *209* (2), 232–236.
- (57) C.L. Chen, D-R. Yost, J.M. Knecht, D.C. Chapman, D.C. Oakley, L. J. M.; J.P. Donnelly, A.M. Soares, V. Suntharalingam, R. Berger, V. Bolkhovsky, W. H.; B.D. Wheeler, C.L. Keast, and D. C. S. Wafer-Scale 3D Integration of InGaAs Image Sensors with Si Readout Circuits. In *2009 IEEE International Conference on 3D System Integration*; 2009.
- (58) Hakkel, K. D.; Petruzzella, M.; Ou, F.; van Klinken, A.; Pagliano, F.; Liu, T.; van Veldhoven, R. P. J.; Fiore, A. Integrated Near-Infrared Spectral Sensing. *Nat. Commun.* **2022**, *13* (103), 1–8.
- (59) Chen, Y.; Liu, J.; Zhao, Y.; Teng, Y.; Hao, X.; Li, X.; Zhu, H.; Zhu, H.; Wu, Q.; Huang, Y. MOCVD Growth of InAs/GaSb Type-II Superlattices on InAs Substrates for Short Wavelength Infrared Detection. *Infrared Phys. Technol.* **2020**, *105* (103209).
- (60) Walther, M.; Schmitz, J.; Rehm, R.; Kopta, S.; Fuchs, F.; Fleißner, J.; Cabanski, W.; Ziegler, J. Growth of InAs/GaSb Short-Period Superlattices for High-Resolution Mid-Wavelength Infrared Focal Plane Array Detectors. *J. Cryst. Growth* **2005**, *278* (1–4), 156–161.

- (61) Sohrabi, L.; Boochani, A.; Sebt, S. A.; Elahi, S. M. Structural , Electronic and Optical Properties of InAs Phases : By GGA-PBG and GGA-EV Approximations. *J. Chem. Res.* **2017**, *41*, 172–182.
- (62) Bechstedt, F.; Belabbes, A. Structure, Energetics, and Electronic States of III-V Compound Polytypes. *J. Phys. Condens. Matter* **2013**, *25* (27).
- (63) Olsson, L. Ö.; Andersson, C. B. M.; Håkansson, M. C.; Kanski, J.; Ilver, L.; Karlsson, U. O. Charge Accumulation at InAs Surfaces. *Phys. Rev. Lett.* **1996**, *76* (19), 3626–3629.
- (64) Richter, M. C.; Mariot, J.; Gafoor, C.; Nicolaï, L.; Heckmann, O.; Djukic, U.; Vobornik, I.; Fujii, J.; Barrett, N.; Feyer, V.; Schneider, C. M.; Hricovini, K. Bi Atoms Mobility-Driven Circular Domains at the Bi / InAs (111) Interface. *Surf. Sci.* **2016**, *651* (111), 147–153.
- (65) Yang, S.; Schröter, N. B. M.; Strocov, V. N.; Schuwalow, S.; Rajpalk, M.; Ohtani, K.; Krogstrup, P.; Winkler, G. W.; Gukelberger, J.; Gresch, D.; Aeppli, G.; Lutchyn, R. M.; Marom, N. Electronic Structure of InAs and InSb Surfaces: Density Functional Theory and Angle-Resolved Photoemission Spectroscopy. *Adv. Quantum Technol.* **2022**, *5* (2100033), 1–13.
- (66) Nakamura, T.; Ohtsubo, Y.; Yamashita, Y.; Ideta, S.; Tanaka, K.; Yaji, K.; Harasawa, A.; Shin, S.; Komori, F.; Yukawa, R.; Horiba, K.; Kumigashira, H.; Kimura, S. Giant Rashba Splitting of Quasi-1D Surface States on Bi/InAs(110)-(2x1). **2018**, No. 110.
- (67) Mårtensson, E. Kinetic and Thermodynamic Modeling of Nanowire Growth, Lund University, 2021.
- (68) Pan, D.; Wang, J.; Zhang, W.; Zhu, L.; Su, X.; Fan, F.; Fu, Y.; Huang, S.; Wei, D.; Zhang, L.; Sui, M.; Yartsev, A.; Xu, H. Q.; Zhao, J. Dimension Engineering of High-Quality InAs Nanostructures on a Wafer Scale. *Nano Lett.* **2019**, *19*, 1632–1642.
- (69) Tersoff, J.; Hamann, D. R. Theory of the Scanning Tunneling Microscope. *Phys. Rev. B* **1985**, *31* (2), 805–813.
- (70) Bardeen, J. Tunnelling from a Many-Particle Point of View. *Phys. Rev. Lett.* **1961**, *6* (2), 57–59.
- (71) Hjort, M. III–V Nanowire Surfaces, Lund University, 2014.
- (72) Chen, C. J. Microscopic View of Scanning Tunneling Microscopy. *J. Vac. Sci. Technol. A* **1991**, *9* (1), 44–50.
- (73) Binnig, G.; Rohrer, H. Scanning Tunneling Microscopy—from Birth to Adolescence. *Rev. Mod. Phys.* **1987**, *59* (3).
- (74) Della Pia, A.; Costantini, G. Scanning Tunneling Microscopy BT - Surface Science Techniques; Bracco, G., Holst, B., Eds.; Springer Berlin Heidelberg: Berlin, Heidelberg, 2013; pp 565–597.
- (75) Kubby, J. A.; Boland, J. J. Scanning Tunneling Microscopy of Semiconductor Surfaces. *Surf. Sci. Rep.* **1996**, *26* (3), 61–204.
- (76) Einstein, A. Über Einen Die Erzeugung Und Verwandlung Des Lichtes Betreffenden Heuristische Gesichtspunkt. *Ann. Phys.* **1905**, *4* (17).

- (77) Hertel, N.; Hoffmann, S. V. ASTRID2: A New Danish Low-Emittance SR Source. *Synchrotron Radiat. News* **2011**, *24* (1), 19–23.
- (78) Walker, R. P. The ELETTRA Synchrotron Radiation Facility. *Rev. Sci. Instrum.* **1992**, *63* (1), 1615–1616.
- (79) Tavares, P. F.; Leemann, S. C.; Sjöström, M.; Andersson, Å. The MAXIV Storage Ring Project. *J. Synchrotron Radiat.* **2014**, *21* (5), 862–877.
- (80) Robinson, A. L. History of Synchrotron Radiation. *Synchrotron Radiat. News* **2015**, *28* (4), 4–9.
- (81) Suga, S.; Sekiyama, A.; Tusche, C. Bulk and Surface Sensitivity of Photoelectron Spectroscopy. In *Photoelectron Spectroscopy: Bulk and Surface Electronic Structures*; Springer International Publishing: Cham, 2021; pp 111–118.
- (82) Shirley, D. A. High-Resolution X-Ray Photoemission Spectrum of the Valence Bands of Gold. *Phys. Rev. B* **1972**, *5* (12), 4709–4714.
- (83) Major, G. H.; Avval, T. G.; Patel, D. I.; Shah, D.; Roychowdhury, T.; Barlow, A. J.; Pigram, P. J.; Greiner, M.; Fernandez, V.; Herrera-Gomez, A.; Linford, M. R. A Discussion of Approaches for Fitting Asymmetric Signals in X-Ray Photoelectron Spectroscopy (XPS), Noting the Importance of Voigt-like Peak Shapes. *Surf. Interface Anal.* **2021**, *53* (8), 689–707.
- (84) *Atomic Calculation of Photoionization Cross-Sections and Asymmetry Parameters*. <https://vuo.elettra.eu/services/elements/WebElements.html> (accessed 2023-07-29).
- (85) Niu, Y.; Vinogradov, N.; Preobrajenski, A.; Struzzi, C.; Sarpi, B.; Zhu, L.; Golias, E.; Zakharov, A. MAXPEEM: A Spectromicroscopy Beamline at MAX IV Laboratory. *J. Synchrotron Radiat.* **2023**, *30*, 468–478.
- (86) Bauer, E. LEEM, SPLEEM and SPELEEM. In *Springer Handbook of Microscopy*; Hawkes, P. W., Spence, J. C. H., Eds.; Springer International Publishing: Cham, 2019; pp 487–535.
- (87) Feng, J.; Scholl, A. Photoemission Electron Microscopy. In *Springer Handbook of Microscopy*; Hawkes, P. W., Spence, J. C. H., Eds.; 2019; pp 537–564.
- (88) Nepijko, S. A.; Schönhense, G. Measurement of Potential Distribution Function on Object Surface by Using an Electron Microscope in the Mirror Operation Mode. *J. Microsc.* **2010**, *238* (1), 90–94.
- (89) Barnett, M. E.; Nixon, W. C. A Mirror Electron Microscope Using Magnetic Lenses. *J. Sci. Instrum.* **1967**, *44* (893).
- (90) Damascelli, A. Probing the Electronic Structure of Complex Systems by ARPES. *Phys. Scr. T* **2004**, *T109*, 61–74.
- (91) Souma, S.; Chen, L.; Oszwaldowski, R.; Sato, T.; Matsukura, F.; Dietl, T.; Ohno, H.; Takahashi, T. Fermi Level Position, Coulomb Gap, and Dresselhaus Splitting in (Ga,Mn)As. *Sci. Rep.* **2016**, *6* (27266), 1–10.
- (92) Hofmann, S. *Auger- and X-Ray Photoelectron Spectroscopy in Material Science*; Springer-Verlag: Berlin, Heidelberg, 2013.
- (93) *Springer Handbook of Microscopy*; Hawkes, P. W., Spence, J. C. H., Eds.; Springer Nature Switzerland AG: Cham, Switzerland, 2019.

- (94) Wolsky, S. P.; Zdanuk, E. J.; Shooter, D. The Sputtering of Compounds. *Surf. Sci.* **1964**, *1*, 110–118.
- (95) Harper, J. M. E.; Berg, S.; Nender, C.; Katardjiev, I. V.; Motakef, S. Enhanced Sputtering of One Species in the Processing of Multielement Thin Films. *J. Vac. Sci. Technol. A Vacuum, Surfaces, Film.* **1992**, *10*, 1765–1771.
- (96) Linnik, S. P.; Buleev, M. A.; Yurasov, V. E.; Zaporozhchenko, V. I.; Chernysh, V. S. Selective Sputtering of Single Crystals of Binary Semiconductor Compounds. *Radiat. Eff.* **1980**, *52*, 191–200.
- (97) Hilner, E.; Lundgren, E.; Mikkelsen, A. Surface Structure and Morphology of InAs(1 1 1)B with/without Gold Nanoparticles Annealed under Arsenic or Atomic Hydrogen Flux. *Surf. Sci.* **2010**, *604* (3–4), 354–360.
- (98) Herrick, C. C. *The Vapor Pressure of Indium*; Los Alamos Scientific Laboratory of the University of California: Los Alamos, 1964.
- (99) Lisak, A.; Fitzner, K. Vapor Pressure Measurements of Arsenic and Arsenic Trioxide over Condensed Phases. *J. Phase Equilibria* **1994**, *15* (2), 151–154.
- (100) Liu, Y.; Benter, S.; Ong, C. S.; Maciel, R. P.; Björk, L.; Irish, A.; Eriksson, O.; Mikkelsen, A.; Timm, R. A 2D Bismuth-Induced Honeycomb Surface Structure on GaAs(111). *ACS Nano* **2022**, *17*, 5047–5058.
- (101) Taguchi, A. First-Principles Investigations of Surface Reconstructions of an InAs (1 1 1) B Surface. *J. Cryst. Growth* **2005**, *278*, 468–472.
- (102) LaBella, V. P.; Krause, M. R.; Ding, Z.; Thibado, P. M. Arsenic-Rich GaAs(0 0 1) Surface Structure. *Surf. Sci. Rep.* **2005**, *60* (1–4), 1–53.
- (103) Dabrowski, M.; Dai, Y.; Hocevar, M.; Frolov, S.; Petek, H. Nanoscale Guiding and Shaping of Indium Droplets. *Appl. Phys. Lett.* **2016**, *109* (261602).
- (104) Hilner, E.; Zakharov, A. A.; Schulte, K.; Kratzer, P.; Andersen, J. N.; Lundgren, E.; Mikkelsen, A. Ordering of the Nanoscale Step Morphology As a Mechanism for Droplet Self-Propulsion. *Nano Lett.* **2009**, *9* (7), 2710–2714.
- (105) Zakharov, A. A.; Mårzell, E.; Hilner, E.; Timm, R.; Andersen, J. N.; Lundgren, E.; Mikkelsen, A. Manipulating the Dynamics of Self-Propelled Gallium Droplets by Gold Nanoparticles and Nanoscale Surface Morphology. *ACS Nano* **2015**, *9* (5), 5422–5431.
- (106) Sanguinetti, S.; Bietti, S.; Koguchi, N. Droplet Epitaxy of Nanostructures. In *Molecular Beam Epitaxy*; Henini, M., Ed.; Elsevier, 2018; pp 293–314.
- (107) Aseev, P.; Wang, G.; Binci, L.; Singh, A.; Martí-Sánchez, S.; Botifoll, M.; Stek, L. J.; Bordin, A.; Watson, J. D.; Boekhout, F.; Abel, D.; Gamble, J.; Van Hoogdalem, K.; Arbiol, J.; Kouwenhoven, L. P.; De Lange, G.; Caroff, P. Ballistic InSb Nanowires and Networks via Metal-Sown Selective Area Growth. *Nano Lett.* **2019**, *19* (12), 9102–9111.
- (108) Mandl, B.; Stangl, J.; Hilner, E.; Zakharov, A. A.; Hillerich, K.; Dey, A. W.; Samuelson, L.; Bauer, G.; Deppert, K.; Mikkelsen, A. Growth Mechanism of Self-Catalyzed Group III-V Nanowires. *Nano Lett.* **2010**, *10* (11), 4443–4449.

- (109) Krogstrup, P.; Popovitz-Biro, R.; Johnson, E.; Madsen, M. H.; Nygård, J.; Shtrikman, H. Structural Phase Control in Self-Catalyzed Growth of GaAs Nanowires on Silicon (111). *Nano Lett.* **2010**, *10* (11), 4475–4482.
- (110) Gurioli, M.; Wang, Z.; Rastelli, A.; Kuroda, T.; Sanguinetti, S. Droplet Epitaxy of Semiconductor Nanostructures for Quantum Photonic Devices. *Nat. Mater.* **2019**, *18*, 799–810.
- (111) Bietti, S.; Basset, F. B.; Tuktamyshev, A.; Bonera, E.; Fedorov, A.; Sanguinetti, S. High-Temperature Droplet Epitaxy of Symmetric GaAs/AlGaAs Quantum Dots. *Sci. Rep.* **2020**, *10* (6532), 1–10.
- (112) Lee, J. H.; Wang, Z. M.; Salamo, G. J. The Control on Size and Density of InAs QDs by Droplet Epitaxy. *IEEE Trans. Nanotechnol.* **2009**, *8* (4), 431–436.
- (113) Anyebe, E. A.; Zhuang, Q.; Sanchez, A. M.; Lawson, S.; Robson, A. J.; Ponomarenko, L.; Zhukov, A.; Kolosov, O. Self-Catalysed Growth of InAs Nanowires on Bare Si Substrates by Droplet Epitaxy. *Phys. Status Solidi - Rapid Res. Lett.* **2014**, *8* (7), 658–662.
- (114) Potts, H.; Morgan, N. P.; Tütüncüoğlu, G.; Friedl, M.; Morral, A. F. I. Tuning Growth Direction of Catalyst-Free InAs(Sb) Nanowires with Indium Droplets. *Nanotechnology* **2017**, *28* (054001).
- (115) Panciera, F.; Baraissov, Z.; Patriarche, G.; Dubrovskii, V. G.; Glas, F.; Travers, L.; Mirsaidov, U.; Harmand, J. C. Phase Selection in Self-Catalyzed GaAs Nanowires. *Nano Lett.* **2020**, *20* (3), 1669–1675.
- (116) Tornberg, M.; Dick, K. A.; Lehmann, S. Branched InAs Nanowire Growth by Droplet Confinement. *Appl. Phys. Lett.* **2018**, *113* (123104).
- (117) Spirina, A. A.; Neizvestny, I. G.; Shwartz, N. L. *Comparative Characteristics of GaAs and InAs Langmuir Evaporation - Monte Carlo Simulation*; 2018; Vol. 386, pp 27–32.
- (118) Benter, S.; Jönsson, A.; Johansson, J.; Zhu, L.; Golias, E.; Wernersson, L. E.; Mikkelsen, A. Geometric Control of Diffusing Elements on InAs Semiconductor Surfaces via Metal Contacts. *Nat. Commun.* **2023**, *14* (4541).
- (119) Gulay, L. D.; Schuster, J. C. Investigation of the Titanium–Indium System. *J. Alloys Compd.* **2003**, *360* (1–2), 137–142.
- (120) Liu, H. S.; Cui, Y.; Ishida, K.; Jin, Z. P. Thermodynamic Reassessment of the Au In Binary System. *Calphad* **2003**, *27* (1), 27–37.
- (121) Okamoto, H. Au-Ga (Gold-Gallium). *J. Phase Equilibria Diffus.* **2013**, *34* (2), 174–175.
- (122) Okamoto, H. Ga-Ti (Gallium-Titanium). *J. Phase Equilibria Diffus.* **2005**, *26* (4), 398.
- (123) Guex, P.; Feschotte, P. Les Systèmes Binaires Platine-Aluminium, Platinegallium et Platine-Indium. *J. Less Common Met.* **1976**, *46* (1), 101–116.
- (124) Tourbot, G.; Bougerol, C.; Grenier, A.; Den Hertog, M.; Sam-Giao, D.; Cooper, D.; Gilet, P.; Gayral, B.; Daudin, B. Structural and Optical Properties of InGaN/GaN Nanowire Heterostructures Grown by PA-MBE. *Nanotechnology* **2011**, *22* (7).

- (125) Feng, Q.; Dong, M.; Gong, R.; Zheng, X.; Liu, B.; Zhang, D.; Feng, Y.; Liu, Y. Heteroepitaxial Growth of GaSb Interfacial Misfit Array on GaAs Substrate by Molecular Beam Epitaxy. *J. Cryst. Growth* **2023**, *616*, 127260.
- (126) Aleksandrova, A.; Golz, C.; Weidlich, H.; Semtsiv, M.; Masselink, W. T.; Takagaki, Y. Ballistic Transport and Surface Scattering in (In,Ga)As-InP Heterostructure Narrow Channels. *Semicond. Sci. Technol.* **2023**, *38* (5), 055017.
- (127) Dominguez, L.; Reyes, D. F.; Bastiman, F.; Sales, D. L.; Richards, R. D.; Mendes, D.; David, J. P. R.; Gonzalez, D. Formation of Tetragonal InBi Clusters in InAsBi/InAs(100) Heterostructures Grown by Molecular Beam Epitaxy. *Appl. Phys. Express* **2013**, *6* (11).
- (128) Zhang, G.; Takiguchi, M.; Tateno, K.; Tawara, T.; Notomi, M.; Gotoh, H. Telecom-Band Lasing in Single InP/InAs Heterostructure Nanowires at Room Temperature. *Sci. Adv.* **2019**, *5* (2), 1–9.
- (129) Kanungo, P. Das; Schmid, H.; Björk, M. T.; Gignac, L. M.; Breslin, C.; Bruley, J.; Bessire, C. D.; Riel, H. Selective Area Growth of III-V Nanowires and Their Heterostructures on Silicon in a Nanotube Template: Towards Monolithic Integration of Nano-Devices. *Nanotechnology* **2013**, *24* (22).
- (130) Messing, M. E.; Wong-Leung, J.; Zanolli, Z.; Joyce, H. J.; Tan, H. H.; Gao, Q.; Wallenberg, L. R.; Johansson, J.; Jagadish, C. Growth of Straight InAs-on-GaAs Nanowire Heterostructures. *Nano Lett.* **2011**, *11* (9), 3899–3905.
- (131) Dey, A. W.; Svensson, J.; Borg, B. M.; Ek, M.; Wernersson, L. E. Single InAs/GaSb Nanowire Low-Power CMOS Inverter. *Nano Lett.* **2012**, *12* (11), 5593–5597.
- (132) Vashishtha, P.; Tanwar, R.; Prajapat, P.; Gangwar, A. K.; Goswami, L.; Singh, P.; Tawale, J.; Dilawar, N.; Gupta, G. Strong Light-Matter Interaction and Antireflection Functionality of f-TiO₂-GaN Heterostructure Broadband Photodetector. *J. Alloys Compd.* **2023**, *948* (169735).
- (133) Lari, L.; Ross, I. M.; Walther, T.; Black, K.; Cheze, C.; Geelhaar, L.; Riechert, H.; Chalker, P. R. GaN-Based Radial Heterostructure Nanowires Grown by MBE and ALD. *J. Phys. Conf. Ser.* **2013**, *471* (1).
- (134) D’Acunto, G.; Shayesteh, P.; Kokkonen, E.; Boix de la Cruz, V.; Rehman, F.; Mosahebfard, Z.; Lind, E.; Schnadt, J.; Timm, R. Time Evolution of Surface Species during the ALD of High-k Oxide on InAs. *Surfaces and Interfaces* **2023**, *39* (May), 102927.
- (135) Geijselaers, I.; Lehmann, S.; Dick, K. A.; Pistol, M.-E. Two-Dimensional Electron Gas at Wurtzite–Zinc-Blende InP Interfaces Induced by Modulation Doping. *Appl. Phys. Lett.* **2020**, *116* (232103).
- (136) Wei, Q.; Wang, H.; Tong, S.; Ma, J.; Zhao, X.; Zhao, J. Ga Composition Effects on the Electrical Parameters of (Al,Ga)Sb/InAs Two-Dimensional Electron Gas. *Semicond. Sci. Technol.* **2020**, *36* (025002).
- (137) Kilpi, O. P.; Andric, S.; Svensson, J.; Ram, M. S.; Lind, E.; Wernersson, L. E. Increased Breakdown Voltage in Vertical Heterostructure III-V Nanowire MOSFETs with a Field Plate. *IEEE Electron Device Lett.* **2021**, *42* (11), 1596–1598.

- (138) Reshak, A. H. Bismuth-Containing Semiconductors GaAs_{1-x}Bi_x for Energy Conversion: Thermoelectric Properties. *Mater. Sci. Semicond. Process.* **2022**, *148* (106850).
- (139) Ferhat, M.; Zaoui, A. Structural and Electronic Properties of III-V Bismuth Compounds. *Phys. Rev. B - Condens. Matter Mater. Phys.* **2006**, *73* (115107), 1–7.
- (140) Benter, S.; Liu, Y.; Maciel, R. D. P.; Ong, C. S.; Linnala, L.; Pan, D.; Irish, A.; Liu, Y.-P.; Zhao, J.; Xu, H.; Eriksson, O.; Timm, R.; Mikkelsen, A. Tuneable 2D Surface Bismuth Incorporation on InAs Nanosheets. *Nanoscale* **2023**.
- (141) Elayech, N.; Fitouri, H.; Boussaha, R.; Rebey, A.; El Jani, B. Calculation of In-As-Bi Ternary Phase Diagram. *Vacuum* **2016**, *131*, 147–155.
- (142) Rösner, B.; Dudin, P.; Bosgra, J.; Hoesch, M.; David, C. Zone Plates for Angle-Resolved Photoelectron Spectroscopy Providing Sub-Micrometre Resolution in the Extreme Ultraviolet Regime. *J. Synchrotron Radiat.* **2019**, *26*, 467–472.
- (143) Dudin, P.; Lacovig, P.; Fava, C.; Nicolini, E.; Bianco, A.; Cautero, G.; Barinov, A. Angle-Resolved Photoemission Spectroscopy and Imaging with a Submicrometre Probe at the SPECTROMICROSCOPY-3.2L Beamline of Elettra. *J. Synchrotron Radiat.* **2010**, *17* (4), 445–450.
- (144) Iwasawa, H. High-Resolution Angle-Resolved Photoemission Spectroscopy and Microscopy. *Electron. Struct.* **2020**, *2* (043001).
- (145) Betti, M. G.; Bertoni, G.; Corradini, V.; De Renzi, V.; Mariani, C. Metal-Induced Gap States at InAs(110) Surface. *Surf. Sci.* **2000**, *454–456*, 539–542.
- (146) Liu, Y.-P. Surfaces and Interfaces of Low Dimensional III-V Semiconductor Devices, Lund University, 2022.
- (147) Kennedy, S. M.; Hjort, M.; Mandl, B.; Marsell, E.; Zakharov, A. A.; Mikkelsen, A.; Paganin, D. M.; Jesson, D. E. Characterizing the Geometry of InAs Nanowires Using Mirror Electron Microscopy. *Nanotechnology* **2012**, *23* (125703).

Acknowledgement

Venturing through a PhD is more of a group effort than a solo trip. I was lucky enough to have more than a handful of people by my side to maneuver through challenging periods but also enjoy this journey together.

First of all, I would like to thank Anders Mikkelsen and Rainer Timm for providing me with this opportunity more than five years ago. I had no actual expectation on how this journey would look like except that I wanted to do interesting experiments. With your supervision I managed to get so much more hands-on, intellectual, and networking experiences, impressions, and adventures than I could have imagined. I highly appreciate your spirits towards our work which made it in the end so much more enjoyable.

Furthermore, thanks to all colleagues at the Synchrotron Radiation Division past and present. From what I gathered over the years, our working climate is quite special. I hope that you can keep this relaxed and engaging atmosphere for a long time to come. In particular I would like to thank Estephania for great support in the STM labs and for keeping things running on a high standard, despite the once-in-a-while grumbling of the equipment or power outage. As several office mates came and went, a constant was always the muffled heavy metal music next door. I highly appreciated sitting next to Patrik as great administrative advice is always very close at hand, and the conversations in the hallway ranging from Sweden's conquest in the (I don't remember which) century to a supposedly free-running lioness in Berlin always pulled me out of the scientific bubble.

Since the main focus of my thesis is more on the characterization side rather than the synthesis, most of the work would not have been possible without our collaborators from China, Dong Pan and Hongqi Xu, as well as from France, Sébastien Plissard, and LTH, Adam Jönsson and Sebastian Lehmann. Thank you for the excellent samples and the interesting scientific discussion. I also want to thank Joanna Millunchik and her research group at the University of Michigan for hosting me for two months in 2019 in Ann Arbor. I felt very welcome from the start and had a very interesting time on the other side of the big pond.

Furthermore, I want to thank several people at various beamlines, facilities and institutions for their great support on-sight, scientific discussion, and taking the time afterwards to help me understand the gathered results: Marcho Bianchi and Philip Hofmann from Aarhus University; Evangelos Golias, Yuran Niu, Craig Polley, Alexei Preobrajenski, Balasubramanian Thiagarajan, Nikolay Vinogradov, Alexei Zakharov and Lin Zhu from Max IV; Matteo Amati, Luca Gregoratti and Paolo Lacovig from Elettra. Special thanks also to Yi, Rohit, Yen-Po and Zephyr with whom I shared most of the 24/7 beamtime experiences and who made the crazy working hours so much more enjoyable and interesting.

Also want to thank all the people working at LINXS for making me feel welcome, always being open to new ideas and great support when things get real. Special thanks also to Anna Hall for helping me detangle my mental jumble and shine light on the important aspects.

This whole experience would have been so much less in every aspect, if it had not been for Ahmed, Rosie, Dima and Sanna, as well as Jack, Virgi, Lukas, Veru, Monica, Peppe, Hanna, Guilio, Valeria and Konstantin. Thanks for making a normal day at the office special, all the get-aways, lovely spontaneous after works, appreciating coffees with ice cream, fikas, laughter, growing and celebrating important moments together, podcast-material conversations, waffle-brunch-lunch-dinners, being my guinea pigs for dessert and soap creations and so much more.

Einen großen Dank auch an meine Familie und Freunde in Deutschland. Nach über sieben Jahren im Ausland bedeutet es mir viel, dass trotz der Entfernung und den leider selteneren Besuchen ich euch immer noch als eins meiner Zuhause bezeichnen kann. Besonders die Motivationsversuche zum Schluss, haben das letzte halbe Jahr erträglicher und auf jeden Fall erheiternder gemacht.



LUND
UNIVERSITY

ISBN 978-91-8039-754-4
Division of Synchrotron Radiation Research
Department of Physics
Faculty of Science
Lund University

